J. Fluid Mech. (2025), *vol.* 1008, A7, doi:10.1017/jfm.2025.35

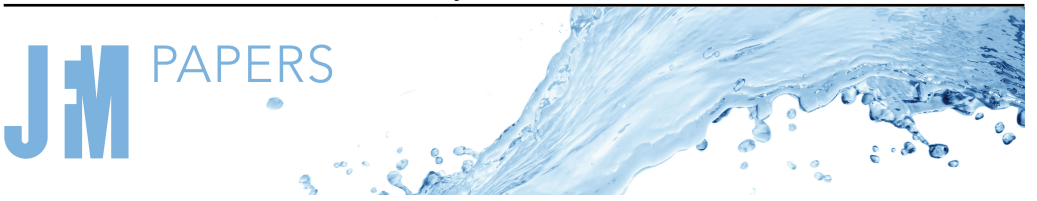

Coriolis effects on wind turbine wakes across neutral atmospheric boundary layer regimes

Kirby S. Heck[1] **and Michael F. Howland**[1]

[1]Department of Civil and Environmental Engineering, Massachusetts Institute of Technology, Cambridge, MA 02139, USA

Corresponding author: Michael F. Howland, mhowland@mit.edu

(Received 17 March 2024; revised 6 December 2024; accepted 3 January 2025)

Wind turbines operate in the atmospheric boundary layer (ABL), where Coriolis effects are present. As wind turbines with larger rotor diameters are deployed, the wake structures that they create in the ABL also increase in length. Contemporary utility-scale wind turbines operate at rotor diameter-based Rossby numbers, the non-dimensional ratio between inertial and Coriolis forces, of $\mathcal{O}(100)$ where Coriolis effects become increasingly relevant. Coriolis forces provide a direct forcing on the wake, but also affect the ABL base flow, which indirectly influences wake evolution. These effects may constructively or destructively interfere because both the magnitude and sign of the direct and indirect Coriolis effects depend on the Rossby number, turbulence and buoyancy effects in the ABL. Using large eddy simulations, we investigate wake evolution over a wide range of Rossby numbers relevant to offshore wind turbines. Through an analysis of the streamwise and lateral momentum budgets, we show that Coriolis effects have a small impact on the wake recovery rate, but Coriolis effects induce significant wake deflections which can be parsed into two regimes. For high Rossby numbers (weak Coriolis forcing), wakes deflect clockwise in the northern hemisphere. By contrast, for low Rossby numbers (strong Coriolis forcing), wakes deflect anti-clockwise. Decreasing the Rossby number results in increasingly anti-clockwise wake deflections. The transition point between clockwise and anti-clockwise deflection depends on the direct Coriolis forcing, pressure gradients and turbulent fluxes in the wake. At a Rossby number of 125, Coriolis deflections are comparable to wake deflections induced by $\sim 20°$ of yaw misalignment.

Key words: atmospheric flows, wakes

© The Author(s), 2025. Published by Cambridge University Press. This is an Open Access article, distributed under the terms of the Creative Commons Attribution-NonCommercial-NoDerivatives licence (https://creativecommons.org/licenses/by-nc-nd/4.0/), which permits non-commercial re-use, distribution, and reproduction in any medium, provided that no alterations are made and the original article is properly cited. The written permission of Cambridge University Press must be obtained prior to any commercial use and/or adaptation of the article.

https://doi.org/10.1017/jfm.2025.35 Published online by Cambridge University Press

1. Introduction

Wind energy is a necessary component for rapid decarbonisation of the global electricity sector (Veers *et al.* 2019). Ambitious climate goals to cut greenhouse gas emissions have led to recent policies propelling the expansion of wind energy development worldwide, particularly for offshore wind (IEA 2022). In parallel, the rated power, hub height and rotor diameter of offshore wind turbines are projected to continue to increase in the foreseeable future (Díaz & Guedes Soares 2020).

Wind turbines, which extract power from the incoming wind, produce momentum and mean kinetic energy deficient regions downwind called wakes. Wind turbine wakes, which are large streamwise flow structures stretching over 10 turbine diameters (D) in length (Högström *et al.* 1988), adversely impact downwind turbines. Lower wind speeds within turbine wakes decrease the power production of waked turbines (Barthelmie *et al.* 2007). For offshore wind farms, wake interactions can reduce annual energy production by 10–20 % (Barthelmie *et al.* 2010), with losses over 30 % possible for very large farms (Pryor *et al.* 2021). Mitigating wake interactions between turbines either through wind farm design or control relies on accurate predictions of wake evolution in the presence of atmospheric boundary layer (ABL) physics (Meyers *et al.* 2022).

All utility-scale wind turbines operate in the ABL, where many physical processes can influence wake evolution, including Coriolis effects. Coriolis forces – which are present in the ABL due to the rotation of the earth – redirect winds and redistribute mean kinetic energy in the atmosphere (Stull 1988). The dynamical importance of Coriolis forces in a rotating flow is described by the Rossby number $Ro = U_c/(\omega_c L_c)$, where U_c is a characteristic velocity scale, ω_c is a characteristic angular velocity and L_c is a characteristic length scale of the flow. The Rossby number represents a ratio of inertial forces to Coriolis forces. Thus, the relative strength of Coriolis forces increases as the characteristic length scale of the flow increases. As wind turbines and, correspondingly, their wakes increase in size, the influence of Coriolis forces on wake evolution, recovery and deflection may differ from the previous generation of wind turbines that have been studied in the existing literature. Furthermore, because wind turbines operate at a range of inflow wind speeds, the relative importance of Coriolis forces on the wake dynamics of a turbine will change across regions of turbine operation as a result of changing U_c. Therefore, it is important to study the effects that Coriolis forces have on wind turbine wake evolution for a range of Rossby numbers.

In the ABL, the characteristic velocity is the geostrophic wind speed G and the angular velocity is the Coriolis parameter $f_c = 2\omega \sin\phi$, where $\omega = 7.29 \times 10^{-5}\,\mathrm{rad\,s^{-1}}$ is the rotation rate of the earth and ϕ is the latitude. The characteristic length scale for wind turbine wake dynamics is the wind turbine diameter D (Vermeulen 1980). As the turbine diameter increases, the relative importance of Coriolis forces increases (Ro decreases). Note that while the turbine diameter is chosen for the characteristic length scale, wind turbine wakes are typically an order of magnitude larger than the turbine diameter (Högström *et al.* 1988). Still, the turbine diameter is selected as the characteristic length scale in the Rossby number because the diameter of a turbine is fixed, while the wake length will depend on properties of the ABL, such as inflow turbulence. Therefore, the definition of the Rossby number used throughout this study is $Ro = G/(f_c D)$.

The presence of Coriolis forces in the ABL has two primary effects on wake development (van der Laan & Sørensen 2017). First, because wind turbine wakes are regions of lower velocity than the surrounding wind flow, the direct Coriolis forcing, which is proportional to the velocity, is different between the wake and the surrounding

https://doi.org/10.1017/jfm.2025.35 Published online by Cambridge University Press

flow (Howland *et al.* 2018). Second, Coriolis forces alter the structure of the background ABL by affecting the vertical shear of wind speed and direction (gradients of wind speed and direction, respectively) (Wyngaard 2010). This background ABL wind, affected by Coriolis forces, flows into the turbine and also influences wake dynamics.

In the previous literature, Coriolis forces have been shown to alter the dynamics of wakes of individual wind turbines and of wind farms. Using large eddy simulation (LES), Abkar & Porté-Agel (2016) studied the wake dynamics of a free-standing wind turbine in the ABL subjected to Coriolis forces (geostrophic pressure gradient forcing) compared with the wake dynamics in a turbulent boundary layer without Coriolis forcing (pressure-driven boundary layer). They found that the presence of Coriolis forces enhances turbulence kinetic energy production driven by wind direction shear (also called 'directional wind shear' or 'wind veer') that is only present in the ABL, which results in faster wake recovery than in the pressure-driven boundary layer without Coriolis forcing. Wind direction shear, caused by Coriolis forcing, also creates a skewed wake structure because different vertical levels of the wind turbine rotor are subjected to different inflow wind directions. In addition to numerical simulations, the skewed wake structure has been observed in field experiments (Magnusson & Smedman 1994; Bodini *et al.* 2017). In summary, the presence of Coriolis forces in the ABL has been shown to alter the recovery and structure of wind turbine wakes relative to wakes in pressure-driven boundary layers.

In addition to changes in the wake recovery and structure, Coriolis effects have been shown to affect wake deflection. In Reynolds-averaged Navier–Stokes (RANS) simulations of a wind farm wake at a diameter-based Rossby number of $Ro = 952$, van der Laan & Sørensen (2017) observed clockwise wake deflection (as viewed from above) as a result of Coriolis effects in the northern hemisphere. They also observed clockwise wake deflection in RANS simulations of an isolated wind turbine wake. The clockwise wake deflection was attributed to the vertical turbulent entrainment of lateral momentum in the wake recovery process, which was shown to add clockwise-turning flow from aloft into the wake region. Winds typically turn clockwise with ascending height in the northern hemisphere due to the Ekman spiral (Ekman 1905), which is caused by Coriolis effects on wind shear in the ABL. In contrast, the direct Coriolis forcing in the wind turbine wake region turns lower velocity wakes anti-clockwise in the ABL (van der Laan & Sørensen 2017; Howland *et al.* 2018). Therefore, for wakes generated in flat, horizontally homogeneous terrain, the vertical entrainment and direct Coriolis forcing mechanisms can be in opposition. The imbalance of the turbulent flux of clockwise-turning momentum over the anti-clockwise direct Coriolis forcing in a wake at $Ro = 952$ has been used to explain the clockwise wake deflections resulting from Coriolis effects (van der Laan & Sørensen 2017).

However, differing results for the magnitude and direction of wake deflection due to Coriolis effects in the ABL have been reported in the existing literature. In LES of a five-row turbine array at $Ro = 1005$, Nouri *et al.* (2020) observed a slight clockwise wake deflection of approximately $0.2D$ at a distance of $6D$ after the first turbine row due to Coriolis effects in the ABL. An investigation of wakes in a stably stratified boundary layer by Englberger *et al.* (2020) at $Ro = 1000$ found that wakes deflect clockwise at hub height, regardless of the rotation direction of the turbine rotor. Additionally, Qian *et al.* (2022) compared lidar and LES data of an offshore wind turbine wake in the ABL at $Ro = 1013$ and observed a similar amount of clockwise wake deflection as Nouri *et al.* (2020). These results agree with the clockwise wake deflection observed by van der Laan & Sørensen (2017). In contrast, other studies have observed zero or anti-clockwise turning in turbine wakes due to Coriolis effects. In LES of a neutrally stratified and stably stratified ABL at $Ro = 574$, Gadde & Stevens (2019) observed an initial anti-clockwise wake deflection of wakes within a wind farm, which transitioned to clockwise deflection after the first

https://doi.org/10.1017/jfm.2025.35 Published online by Cambridge University Press

2–3 rows of turbines. They noted that the transition to clockwise deflection was related to the vertical turbulent momentum flux into the wake region. Negligible wake deflection was reported in single-turbine studies using RANS (Van Der Laan *et al.* 2015) and LES (Abkar *et al.* 2018; Mohammadi *et al.* 2022) for Rossby numbers between 550 and 1200. Finally, anti-clockwise wake turning was observed in LES of offshore wind farms by Dörenkämper *et al.* (2015) in land–sea transition at $Ro = 815$ and by Allaerts & Meyers (2017) in neutrally stratified conditions at $Ro = 1200$.

Several challenges are highlighted by the spread of wake deflection results in the previous literature. For example, insufficient time averaging can conflate wake deflection results with unsteady ABL turbulence, as noted by Churchfield *et al.* (2016). Additionally, wind speed and direction shear depend on the strength of Coriolis forcing relative to the strength of inertial forces in the ABL (throughout this paper, relative Coriolis forcing strength refers to the comparison between inertial forces and Coriolis forces, as quantified by the Rossby number). Because neutral boundary layers are sensitive to their heating history (Tennekes 1973; Allaerts & Meyers 2017), wind shear and turbulence, which affect the wake deflection, can vary significantly for the same Rossby number. For stable boundary layers, wind shear and turbulence also vary based on the surface cooling rate, which is independent of the Rossby number. Unless these factors are controlled, comparisons of wake dynamics in ABL conditions may have contradictory results.

Previous literature has also focused on a relatively narrow range of Rossby numbers between $Ro = 550$ and $Ro = 1200$. For the National Renewable Energy Laboratory (NREL) 5-MW reference turbine (Jonkman *et al.* 2009) with a 126-m rotor diameter, this represents a wind speed range of $6.5-13\ \mathrm{m\ s^{-1}}$ in the mid-latitudes. However, trends to both manufacture larger turbines (increasing D) as well as install new wind turbines in regions of lower average wind speed (decreasing G) push turbines into lower Rossby number regimes. For example, the International Energy Agency (IEA) 15-MW reference turbine (Gaertner *et al.* 2020) has a 240-m rotor diameter, nearly twice as large as the NREL 5 MW. In contrast to the NREL 5-MW turbine, which produces rated power at $Ro = 880$ in the mid-latitudes, the IEA 15-MW reference turbine rated wind speed corresponds to $Ro = 430$ where the ratio of Coriolis to inertial forces is twice as large. Meanwhile, the IEA 15-MW turbine cut-in occurs at $Ro = 120$. Recently, a 22-MW reference turbine with a 280-m rotor diameter was published by the IEA (Zahle *et al.* 2024). Figure 1 shows this trend for larger offshore wind turbines to operate in lower Rossby number regimes – which will be investigated in this study – overlaid on a survey of prior numerical studies on turbine wakes including Coriolis forces.

The existing body of literature addressing Coriolis effects on wake evolution focuses on Rossby numbers pertinent to the previous generation of wind turbines. Larger turbines will operate in Rossby number regimes where ABL dynamics may differ from the Rossby number regimes at which present-day wind turbines operate, but the demarcation of different regimes is not clear from the existing literature. In this study, we explore a wide range of Rossby numbers relevant to flows at the contemporary commercial turbine scale. In particular, we consider the range of Rossby numbers relevant to the IEA 15-MW reference turbine. For this turbine in the mid-latitudes ($\phi = 45°$), Rossby numbers between 100 and 500 span the range of wind speeds in regions I and II of wind turbine control – where wake interactions are most relevant – as shown in figure 1.

Here, we present a suite of large eddy simulations of increasing complexity that parametrically vary the relative strength of Coriolis forcing. Three types of inflow are considered. First, wake dynamics is investigated in turbulence-free, shear-free uniform inflow to isolate the direct Coriolis forcing on the wake from the Coriolis effects on the wind shear. Then, wind turbine wakes are simulated in neutrally stratified boundary layers

https://doi.org/10.1017/jfm.2025.35 Published online by Cambridge University Press

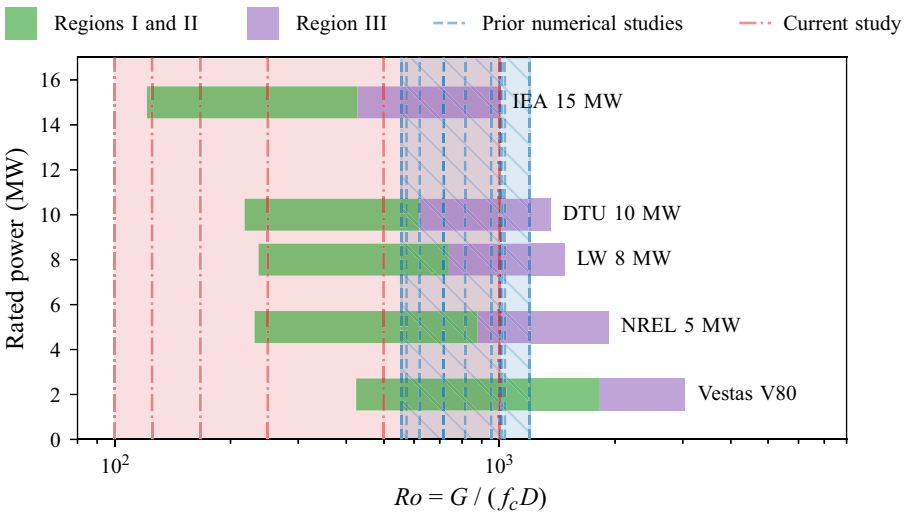

Figure 1. Relevant Rossby numbers for several wind turbine models in the mid-latitudes ($\phi = 45°$). Green bars indicate Region I and II operation where turbines aim to maximise the power they extract from the wind, while purple bars indicate Region III operation where individual turbines curtail power generation at high wind speeds. Previous numerical experiments are marked with blue dashed lines, and simulations from the current study are shown as red dash-dotted lines.

to study both the direct Coriolis forcing and Coriolis effects on wind shear which influence wake dynamics. Finally, we simulate wakes in conventionally neutral conditions, where the neutral boundary layer is capped by a stable free atmosphere. We focus on neutral boundary layers in this work to limit the problem complexity and to isolate the competing direct and indirect effects of Coriolis forcing on wake evolution. In each of these inflow conditions, we examine the primary momentum transport mechanisms governing wake recovery, deflection and structure as a function of the Rossby number. The goal is to understand how Coriolis effects influence wake evolution across the range of Rossby numbers that will be encountered by existing and future wind turbines.

The remainder of this study is organised as follows. In § 2, we introduce the LES numerical set-up. Following this, in § 3, we present a streamtube-based methodology for analysing the time-averaged wake recovery, deflection and dynamics. Results are shown in § 4 for the inflow conditions, wake structure and evolution, and momentum budget analysis, followed by concluding remarks and discussion of future work in § 5.

2. LES numerical set-up

In this study, large eddy simulations are used to solve the non-dimensional, filtered, incompressible Navier–Stokes equations under the infinite Reynolds number limit with the Boussinesq approximation for buoyancy,

$$\frac{\partial \tilde{u}_i}{\partial x_i} = 0, \tag{2.1}$$

$$\frac{\partial \tilde{u}_i}{\partial t} + \tilde{u}_j \frac{\partial \tilde{u}_i}{\partial x_j} = -\frac{\partial \tilde{p}^\star}{\partial x_i} + \frac{\delta_{i3}}{\theta_0 Fr^2}(\tilde{\theta} - \langle\tilde{\theta}\rangle_{xy}) - \frac{\partial \tau^d_{ij}}{\partial x_j} - \frac{1}{Ro}\varepsilon_{ij3}(G_j - \tilde{u}_j) + f_{t,i}, \tag{2.2}$$

where $\tilde{u}_i$ is the filtered non-dimensional velocity in the x_i direction, t is non-dimensional time and $\tilde{\theta}$ is the filtered potential temperature. The $i = 1, 2$ and 3 indices correspond

https://doi.org/10.1017/jfm.2025.35 Published online by Cambridge University Press

with the streamwise (x), lateral (y) and vertical (z) directions, respectively. The non-dimensional turbine forcing is given by $f_{t,i}$ and subgrid stresses are given by τ_{ij}, of which the deviatoric components are $\tau_{ij}^d = \tau_{ij} - \delta_{ij}\tau_{kk}/3$. The filtered non-dimensional modified pressure $\tilde{p}^\star$ absorbs the trace of the subgrid stresses: $\tilde{p}^\star = \tilde{p} + \tau_{kk}/3$. The reference potential temperature is θ_0, δ_{ij} is the Kronecker delta, ε_{ijk} is the permutation operator and $\langle\cdot\rangle_{xy}$ denotes horizontal averaging. Note that the geostrophic balance has been substituted such that the $(1/Ro)\,\varepsilon_{ij3}G_j$ term represents the geostrophic pressure gradient and G_j is the geostrophic velocity vector. Following the definition of the Rossby number in § 1, the velocity scale is G and the characteristic length scale is the turbine diameter D, which are used to non-dimensionalise the velocity, spatial coordinate, pressure and time variables. The Froude number $Fr = G/\sqrt{gD}$ governs the magnitude of buoyancy forces, where g is the gravitational acceleration. Only the vertical component of Earth's rotation is included in this study (Stull 1988). The prognostic equation for the filtered potential temperature $\tilde{\theta}$ is given by

$$\frac{\partial\tilde{\theta}}{\partial t} + \tilde{u}_j\frac{\partial\tilde{\theta}}{\partial x_j} = \frac{\partial q_j}{\partial x_j}, \tag{2.3}$$

where q_j is the subgrid-scale heat flux. The incompressible flow solver PadéOps (https://github.com/Howland-Lab/PadeOps) (Ghate & Lele 2017; Howland *et al.* 2020) is used to solve the filtered incompressible Navier–Stokes equations. Details on the numerical flow solver are given in Appendix A. Tildes are omitted in the remainder of the manuscript (with the exception of Appendix A) for simplicity of notation.

An actuator disk model (ADM) wind turbine is used to represent the momentum sink at the rotor (Calaf *et al.* 2010; Shapiro *et al.* 2019). Details of the ADM numerical set-up are given in Appendix A.1. The turbine size is based on the IEA 15-MW reference turbine (Gaertner *et al.* 2020). The diameter of the reference turbine is $D = 240$ m and the turbine hub height is $z_h = 150$ m. The range of rotor diameter-based Rossby numbers that span the operational range of the IEA 15-MW reference turbine in the mid-latitudes ($\phi = 45°$) are $Ro = 120$ at the cut-in speed of $3\ \mathrm{m\ s^{-1}}$ and $Ro = 430$ at the rated wind speed of $10.6\ \mathrm{m\ s^{-1}}$. To vary the relative strength of Coriolis forcing, the Rossby number is changed for each independent simulation. Below rated wind speed, the thrust coefficient C_T' is nearly constant (Gaertner *et al.* 2020). We choose a constant $C_T' = 1.33$ for all Rossby numbers (and wind speeds, including those below cut-in), rather than following the thrust curve of the IEA 15-MW reference turbine, to focus this study on the effect of Coriolis forces on wake dynamics. Choosing a constant C_T' also improves the generalisability of the results across turbine models. We sweep over a range of Rossby numbers by varying Ro^{-1} linearly from 0.002 ($Ro = 500$) to 0.010 ($Ro = 100$). This parameter range overlaps with region II operation of the IEA 15-MW reference turbine (Gaertner *et al.* 2020) as shown in figure 1. Additionally, simulations at $Ro = 1000$ are included to compare with the existing literature. We note that because of the non-dimensionalisation of the Coriolis forcing, the Rossby numbers studied here can be mapped to different wind speed ranges of other turbine diameters or at different latitudes.

All simulations are performed with a computational domain of length $L_x = 38.4D$ (9.2 km) in the streamwise direction and a cross-section $L_y \times L_z$ of $12.8D \times 12.8D$ (3.1 km × 3.1 km) unless noted otherwise. The domain is rectangular and uses an evenly spaced, uniform grid of $384 \times 256 \times 256$ points, resulting in 19 points in the vertical direction across the ADM, which is sufficient resolution for convergence of turbine forcing (Stevens *et al.* 2018). The ADM is placed $5D$ from the inlet of the computational domain.

https://doi.org/10.1017/jfm.2025.35 Published online by Cambridge University Press

Simulations are run until time-averaged statistics within the wind turbine wake have converged, which varies based on the dynamics of the problem set-up. Three different problem set-ups of increasing complexity are described in §§ 2.1 and 2.2 to study the influence of Coriolis forces on wind turbine wakes.

2.1. *Uniform inflow simulation set-up*

A wind turbine wake in uniform turbulence-free inflow serves as the canonical reference case to study interactions between wakes and Coriolis effects. In uniform inflow simulations, transport mechanisms related to Coriolis forces can be isolated without confounding variables such as free stream turbulence, wind shear or thermal stratification. A single ADM turbine is centred laterally and vertically in the computational domain, and the bottom and top domain boundaries are slip walls. The velocity is initialised to the geostrophic wind velocity in the x direction in the entire domain and the geostrophic wind speed is set based on the Rossby number Ro. There is no velocity shear, no thermal stratification and zero turbulence in the prescribed inflow. The prognostic equation for the potential temperature is omitted in the uniform inflow simulations. Time-averaged statistics are taken over an interval of eight flow-through times ($8L_x/G$), which is sufficient for turbulence-free uniform inflow simulations (Howland *et al.* 2016). An initial transient period of $2L_x/G$ allows a buffer time for the wake to develop before averaging begins.

2.2. *Atmospheric boundary layer simulation set-up*

In the ABL, Coriolis forcing has a direct effect on wake evolution, as in the uniform inflow case, but also has indirect effects that manifest through wind shear. Both of these effects depend on the Rossby number. Additionally, buoyancy effects modify wind shear and turbulent fluxes in the ABL (Stull 1988). Thermal stratification, which may be stable, neutral or unstable (convective), also alters wake evolution (Abkar & Porté-Agel 2015; Xie & Archer 2017). We simulate neutrally stratified ABLs, which have no vertical potential temperature gradient in the boundary layer region, to study the effects of Coriolis forcing on wake development while minimising additional complexity due to buoyancy effects. Two types of neutrally stratified ABLs are studied. The truly neutral boundary layer (TNBL), also known as the turbulent Ekman layer (Ekman 1905), is neutrally stratified throughout the vertical domain. That is, the TNBL is isothermal. Initialisation for the TNBL is described in § 2.2.1. While no atmospheric boundary layers are truly neutral due to the presence of stable stratification in the free atmosphere (Stull 1988), parametrically analysing the influence of Coriolis forcing on wind turbine wakes in the TNBL adds the complexity of wind speed and direction shear without considering the effects of thermal stratification. We also simulate conventionally neutral boundary layer (CNBL) inflow (Zilitinkevich *et al.* 2007). The CNBL adds a stably stratified free atmosphere above a neutrally stratified, turbulent boundary layer, which is more similar to neutral ABLs observed in the environment (Rampanelli & Zardi 2004). The initialisation for the CNBL potential temperature field is given in § 2.2.2.

After initialising the potential temperature field, pseudo-random potential temperature perturbations are added to the bottom 100 m of the ABL to spin-up turbulence. The initial velocity profile is uniform and geostrophic, aligned in the x-direction. The bottom boundary condition uses a Monin–Obukhov wall model (Moeng 1984) with a surface roughness $z_0 = 0.1$ mm, which is characteristic of offshore wind conditions (Stull 1988; Allaerts & Meyers 2017). The heat flux at the ground is set to zero to enforce neutrally stratified conditions in the ABL. A Rayleigh damping layer (RDL) (Klemp & Lilly 1978)

https://doi.org/10.1017/jfm.2025.35 Published online by Cambridge University Press

is used in the upper 25% of the vertical domain to absorb perturbations propagated into the free atmosphere. Additional numerical details regarding the boundary conditions, wall model and RDL are provided in Appendix A. The spin-up simulation is run until $t = 15/f_c \approx 40$ h to allow inertial oscillations to decay such that the ABL reaches statistical quasi-equilibrium.

Before placing a turbine in the ABL, the flow at hub height is aligned to the x-direction by rotating the domain in the spin-up simulation with a wind angle controller which imparts a pseudo-Coriolis force (Sescu & Meneveau 2014; Howland *et al.* 2020). The rotation only aligns the flow with the computational domain and does not affect the ABL structure or statistics (Sescu & Meneveau 2014; Howland *et al.* 2018). Once the wind angle is rotated and the boundary layer reaches a new equilibrium, the wind angle controller is turned off. Because the ABL is in quasi-equilibrium at the end of the spin-up simulation, the wind angle drift is small and the hub height wind angle remains within $\pm 1^\circ$ of the original direction for all simulations after the wind angle controller is removed. Sensitivity to wind angle drift is given in Appendix A.5.

The concurrent-precursor method (Stevens *et al.* 2014) is used to simulate a finite wind turbine wake. An ADM turbine is placed in the boundary layer at a hub height of $z_h = 150$ m and centred laterally in the domain of the primary simulation. The ADM does not use a yaw angle controller because the wind angle drift is small, so the wind turbine remains approximately yaw-aligned throughout the simulation. As a result, the turbine forcing remains exclusively in the x-direction. A fringe region is active for the primary simulation only, which restores the flow to the state of the precursor simulation. Additional numerical details on the concurrent set-up are provided in Appendix A.2. We find that the sensitivity of the time-averaged streamwise velocity fields due to the numerical set-up of the concurrent simulations is less than 1.5 %, which does not significantly affect our results. The concurrent simulations are time-averaged over one inertial period $T = 2\pi/f_c \approx 17$ h to allow wake statistics to converge, and to avoid averaging over a partial period of inertial oscillations. This is a sufficiently long time-averaging window as shown in Appendix B. A transient period of $2L_x/G$ is again used for the wake to develop before averaging begins.

2.2.1. *TNBL initialisation*

In the TNBL, also known as the Ekman layer (Ekman 1905), thermal stratification is absent throughout the entire domain. The TNBL potential temperature profile is initialised with $\theta(z) = \theta_0$, where $\theta_0 = 300$ K for all simulations. The domain height L_z is selected such that the TNBL development is unaffected by the vertical domain constraint. We choose L_z such that $L_z > 2.5h_E$ to minimise the domain dependence on TNBL development (Goit & Meyers 2015; Jiang *et al.* 2018), where $h_E \approx 0.6u_*/|f_c|$ is the Rossby–Montgomery equilibrium height (Rossby & Montgomery 1935). For the $Ro = 500$ and $Ro = 1000$ simulations of the TNBL, the vertical domain is expanded to $L_z = 19.2D$ (=4.6 km) and $L_z = 38.4D$ (=9.2 km), respectively, to accommodate the boundary layer growth. The number of grid points is also increased to 384 and 768, respectively, to keep the vertical grid spacing Δz equal to all other simulations.

2.2.2. *CNBL initialisation*

For simulations of the CNBL (Zilitinkevich *et al.* 2007), the ABL profile is initialised following the procedure of Liu *et al.* (2021). An initial linear potential temperature profile $\theta(z) = \theta_0 + \Gamma z$ is used, where Γ is the free atmosphere lapse rate. For all CNBL simulations, $\theta_0 = 300$ K and $\Gamma = 1$ K km^{-1}, simulating a weakly stratified free

https://doi.org/10.1017/jfm.2025.35 Published online by Cambridge University Press

atmosphere (Sorbjan 1996). Unlike the TNBL simulations, the stable free atmosphere in the CNBL suppresses the ABL height and forms a weak capping inversion. A relatively weak lapse rate is chosen to mitigate the interaction of the turbine directly with the free atmosphere for low Rossby numbers. Additionally, for the $Ro = 1000$ simulation in the CNBL, the vertical domain height is expanded to $L_z = 19.2D$ (=4.6 km) to accommodate boundary layer growth.

3. Momentum budget analysis

To understand the structure and evolution of wakes in the ABL, we analyse the time-averaged streamwise and lateral momentum budgets. This will help to connect observations of wake recovery and wake deflection with the ABL forcings present in the governing equations. In § 3.1, the time-averaged RANS equations are presented, and nomenclature is defined to refer to different forcing terms in the wake and ABL. Following this, in § 3.2, a streamtube is defined to follow the wind turbine wake region, and the streamtube-averaged momentum budgets are presented to interpret the dynamics governing wake evolution and recovery.

3.1. *Steady RANS equations*

To arrive at the filtered RANS equations, we apply the Reynolds decomposition to (2.2) to separate the time-averaged $\overline{(\cdot)}$ and fluctuating components (e.g. $u_i = \bar{u}_i + u_i'$). Assuming statistically steady flow ($\partial(\cdot)/\partial t = 0$), applying the Reynolds decomposition and time-averaging yields

$$\bar{u}_j \frac{\partial \bar{u}_i}{\partial x_j} = -\frac{\partial \bar{p}^\star}{\partial x_i} + \frac{\delta_{i3}}{\theta_0 Fr^2}(\bar{\theta} - \langle\bar{\theta}\rangle_{xy}) - \frac{\partial \bar{\tau}_{ij}^d}{\partial x_j} - \frac{1}{Ro}\varepsilon_{ij3}(G_j - \bar{u}_j) + \bar{f}_{t,i} - \frac{\partial \overline{u_i' u_j'}}{\partial x_j}. \tag{3.1}$$

Note that in steady state, only the advective contribution remains in material derivative $D/Dt = (\partial/\partial t + \bar{u}_j \partial/\partial x_j)$. The final term in (3.1) is the divergence of the grid-resolved Reynolds stresses $\overline{u_i' u_j'}$, which can be interpreted as a turbulent flux of momentum.

The wake recovery, quantified by the evolution of the streamwise velocity downwind of the turbine, is governed by the RANS equation in the streamwise ($i = 1$) direction. In the wake away from the turbine, the turbine forcing $\bar{f}_{t,i}$ is zero and the streamwise RANS equations yield

$$\underbrace{\bar{u}_j \frac{\partial \bar{u}}{\partial x_j}}_{\text{I}} = \underbrace{-\frac{\partial \bar{p}^\star}{\partial x}}_{\text{II}} \underbrace{-\frac{1}{Ro}(G_2 - \bar{v})}_{\text{III}} \underbrace{-\frac{\partial \overline{u' u_j'}}{\partial x_j}}_{\text{IV}} \underbrace{-\frac{\partial \bar{\tau}_{1j}^d}{\partial x_j}}_{\text{V}}, \tag{3.2}$$

where $(u_1, u_2, u_3) = (u, v, w)$ is used to refer to the velocities in the streamwise, lateral and vertical directions, respectively. The bracketed terms are: (I) mean advection of streamwise momentum; (II) streamwise modified pressure gradient force; (III) sum of geostrophic pressure gradient force and direct Coriolis force; (IV) turbulent flux of streamwise momentum and (V) divergence of subgrid stresses. In the analysis and results, we abbreviate term (II) as the modified pressure forcing and term (III) as the wake Coriolis term. The lateral geostrophic wind component $G_2 = G\sin(\alpha)$ is non-zero because the domain is rotated by angle α to align the hub height inflow with the x direction due to the Ekman spiral (Ekman 1905).

https://doi.org/10.1017/jfm.2025.35 Published online by Cambridge University Press

Wake deflection is governed by the wake and ABL dynamics in the lateral ($i = 2$) RANS equation. Lateral forcing in the wake leads to lateral wake acceleration, which induces non-zero $\bar{v}$ within the wake and causes wake deflection. The RANS equation for the lateral direction is given by

$$\underbrace{\bar{u}_j \frac{\partial \bar{v}}{\partial x_j}}_{\text{I}} = \underbrace{-\frac{\partial \bar{p}^\star}{\partial y}}_{\text{II}} \underbrace{+\frac{1}{Ro}(G_1 - \bar{u})}_{\text{III}} \underbrace{-\frac{\partial \overline{v'u'_j}}{\partial x_j}}_{\text{IV}} \underbrace{-\frac{\partial \bar{\tau}^d_{2j}}{\partial x_j}}_{\text{V}}, \tag{3.3}$$

where the bracketed terms are: (I) mean advection of lateral momentum; (II) lateral modified pressure gradient force; (III) sum of geostrophic pressure gradient force and direct Coriolis force; (IV) turbulent flux of lateral momentum and (V) subgrid stress divergence. Again, term (II) is labelled modified pressure forcing and term (III) is shortened to wake Coriolis for concision. In the canonical case of a turbulent wake in a pressure-driven boundary layer without Coriolis forcing, the flow is symmetrical across the lateral (y) direction and the lateral pressure gradient averages to zero across the wake region (Pope 2000). The addition of Coriolis forces breaks the wake symmetry and the lateral pressure gradients cannot necessarily be neglected.

3.2. *Streamtube-averaged quantities*

To translate between observations of wake evolution and the wake momentum budgets, we define and track a streamtube containing the mass that intersects the rotor disk. We note that the streamtube framework has been extended by Meyers & Meneveau (2013) to follow parcels of momentum and energy in a similar perspective, but we limit our scope to the conventional streamtube in this analysis. The streamtube boundary is defined as the bundle of streamlines that passes through a ring of radius $r_s = 0.4D$ centred around and in the plane of the ADM (e.g. Shapiro *et al.* 2018). A schematic of a streamtube is shown in figure 2(*a*). A larger streamtube ($r_s \sim 0.5D$) encapsulates a greater portion of the wake. In contrast, the wake dynamics and the background ABL flow, which is affected by wind shear, will be more homogeneous inside a smaller streamtube. Further, the edges of the streamtube for $r_s = 0.5D$ will be sensitive to the ADM regularisation method, which smooths out the actuator disk forcing on the numerical grid (Shapiro *et al.* 2019). As a compromise, we select $r_s = 0.4D$, but we note that the qualitative results are insensitive to the choice of initial streamtube radius, which is discussed in Appendix C. Additionally, we present the wake centroid position $y_c(x)$ by computing the centroid of the streamtube cross-section Ω, as shown in figure 2(*b*). The streamtube centroid is computed by its geometric centre at each x location ($y_c = \iint_\Omega y \, \mathrm{d}y \, \mathrm{d}z / \iint_\Omega \mathrm{d}y \, \mathrm{d}z$). Other definitions of the wake centroid (cf. Howland *et al.* 2016) yield the same qualitative results, which is also discussed in Appendix C. Streamlines in the streamtube are computed by integrating the locus of starting points along the velocity field $\bar{u}_i(x, y, z)$. Because streamlines follow the time-averaged flow, no mass crosses the streamtube boundary. As a result, the mass flux through any yz cross-section of the streamtube (the region shown in figure 2*b*) is constant.

In this work, we choose to study the wake dynamics by analysing a streamtube seeded at the turbine rotor which follows the turbine wake. This choice is helpful for several reasons. First, the streamtube boundary represents a physically meaningful region that robustly follows the wake structure and evolution. The streamtube is an analogue for the wake, tracking the wake position and wake deformation. Second, the momentum budgets can be connected to the observed wake behaviour (e.g. wake deflection) with the streamtube. For a given parcel of air in a Lagrangian frame of reference, a streamline trajectory can be recovered from an initial velocity and position by integrating the right-hand side of

https://doi.org/10.1017/jfm.2025.35 Published online by Cambridge University Press

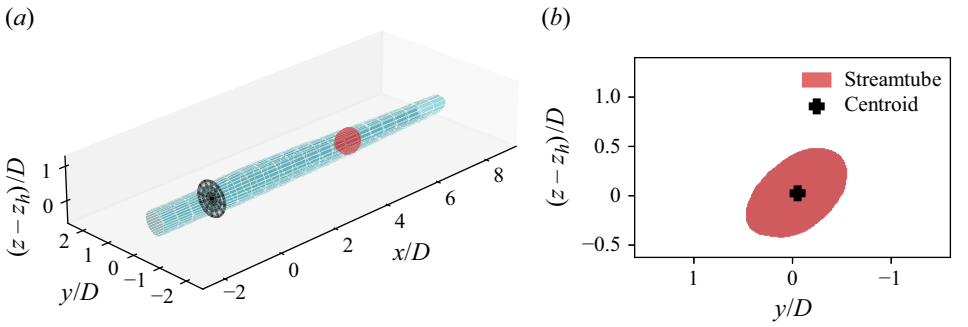

Figure 2. Schematic describing the streamtube boundary. (*a*) A streamtube for TNBL inflow at $Ro = 250$ wake is shown, seeded at the actuator disk with radius $r_s = 0.4D$. (*b*) A slice out of the streamtube shows the averaging region and centroid location.

(3.1) in time, which is derived in Appendix D. In this way, the trajectory of the parcel is an integrated form of the forcing terms in the momentum equations. The same principle applies to a bundle of streamlines which describes a streamtube. Third, the streamwise spatial evolution of field variables and budget quantities is easier to interpret for averaged quantities than for disaggregated profiles or planes. We choose to average quantities in the yz-plane within the streamtube to describe the mean dynamics within the wake as a function of the streamwise direction x, and yz-averaging within the streamtube is denoted $\langle\cdot\rangle$. Additionally, quantities that are averaged or integrated over the streamtube region are less sensitive to parameters in the streamtube definition (e.g. where the streamtube is seeded) than over a rectangular domain enclosing the wake region, for which we find averaged quantities to be sensitive to both the choice of lateral and vertical domain boundaries. For these reasons, streamtube-averaged quantities will be used to describe the evolution of the wake in the presence of Coriolis effects. Further discussion of the sensitivity of the reported wake dynamics results to various methods of post-processing are given in Appendix C.

4. Results

The results section begins in § 4.1 with the inflow profiles for uniform, TNBL and CNBL conditions as a function of the relative Coriolis forcing strength, as quantified by the Rossby number. Then, we highlight the qualitative dependence of wake evolution for varying relative Coriolis strength in § 4.2. The wake dynamics of the uniform inflow problem set-up are analysed in § 4.3, before transitioning to the analysis of wake dynamics in ABL inflow in §§ 4.4 and 4.5. Finally, we conclude the results section in § 4.6 with a discussion of the statistical significance and relevance of Coriolis effects on wind turbine wakes in the context of wind farm design and control.

4.1. *Precursor simulations*

Profiles for the horizontally averaged wind speed, wind direction, temperature and turbulence intensity from the precursor simulations are shown in figure 3. Turbulence intensity is defined as $TI = ((2/3)\langle\bar{k}^B\rangle_{xy})^{1/2}/U$, where $\bar{k}$ is the time-averaged resolved turbulence kinetic energy, $\langle\cdot\rangle_{xy}$ denotes horizontal averaging and the superscript B denotes the base flow without turbines. The horizontally averaged wind speed magnitude is given by $U = (\langle\bar{u}^B\rangle_{xy}^2 + \langle\bar{v}^B\rangle_{xy}^2)^{1/2}$. In the uniform inflow simulations, shown in figure 3(*a–d*), inflow profiles are independent of the Rossby number. This is due to the absence of velocity

https://doi.org/10.1017/jfm.2025.35 Published online by Cambridge University Press

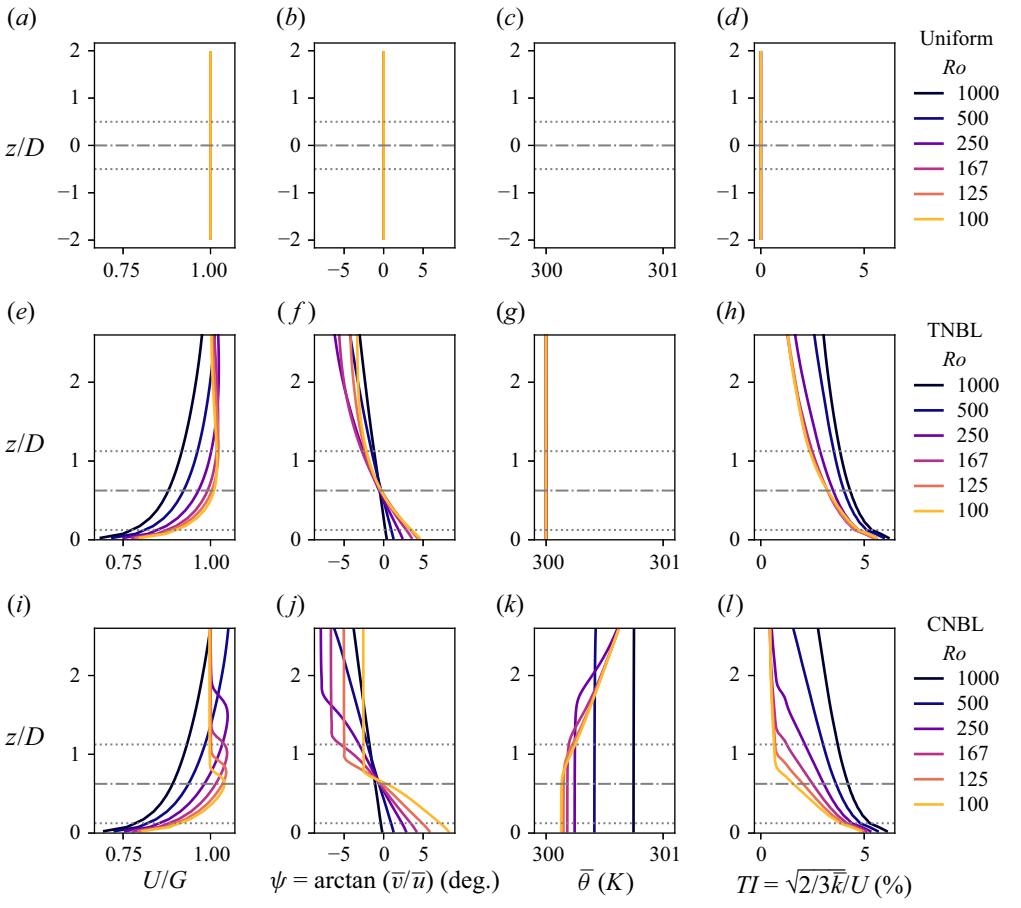

Figure 3. Horizontally and time-averaged inflow profile characteristics under (*a–d*) uniform, (*e–h*) truly neutral (TNBL) and (*i–l*) conventionally neutral (CNBL) conditions. The turbine hub height z_h is shown by the dash-dotted line, and the top and bottom extents of the rotor are shown by the dotted lines. Note that a prognostic equation for the potential temperature is not solved for the uniform inflow conditions.

shear in uniform inflow and a domain with slip-walls. Note that the vertical domain extent is much larger than the profiles shown in figure 3, which are zoomed in to the rotor area.

Adding a bottom wall introduces velocity shear and thus vertical variation in the inflow profiles as a function of the Rossby number for the ABL simulations, shown in figure 3(*e–l*). In the TNBL, the wind speed magnitude U increases to a maximum of $U_{max} \approx 1.02G$ at the low-level jet. The non-dimensional friction velocity u_*/G shows a weak inverse dependence on the Rossby number, and a summary of inflow and ABL properties is given in table 1. The height of the ABL depends on the Rossby number by the Rossby–Montgomery equilibrium height (Rossby & Montgomery 1935; Zilitinkevich *et al.* 2007). In table 1, we compute the ABL height h as the vertical height where the turbulent fluxes reach 5% of their surface value (Zilitinkevich *et al.* 2007). We note that h changes considerably across the range of Rossby numbers simulated and we keep z_h constant rather than fixing the dimensionless ratio z_h/h. Additional simulations with constant z_h/h are provided in Appendix E to control this dimensionless parameter, and the results show the same qualitative response in the wake dynamics dependent on Ro as for fixed $z_h = 150$ m. The magnitude of wind direction shear at the surface monotonically

https://doi.org/10.1017/jfm.2025.35 Published online by Cambridge University Press

Flow type	G (m s^{-1})	Ro (–)	u_*/G (–)	h (m)	ψ_{hub} (°)	u_{hub}/G (-)	U_{max}/G (-)	$\Delta\psi$ (°)
Uniform	24.7	1000	-	–	0	1	1	0
	12.4	500	-	–	0	1	1	0
	6.2	250	-	–	0	1	1	0
	4.1	167	-	–	0	1	1	0
	3.1	125	-	–	0	1	1	0
	2.5	100	-	–	0	1	1	0
TNBL	24.7	1000	0.0252	3057	−0.50	0.88	1.02	−1.4
	12.4	500	0.0264	1673	−0.32	0.92	1.02	−2.5
	6.2	250	0.0274	831	−0.56	0.97	1.02	−4.5
	4.1	167	0.0283	604	−0.41	0.99	1.02	−5.6
	3.1	125	0.0288	493	−0.28	1.00	1.02	−5.7
	2.5	100	0.0293	477	−0.37	1.01	1.02	−5.7
CNBL	24.7	1000	0.0250	1359	−1.07	0.89	1.05	−1.5
	12.4	500	0.0263	717	−0.60	0.94	1.05	−3.0
	6.2	250	0.0277	390	−0.48	0.98	1.05	−5.4
	4.1	167	0.0285	272	−0.50	1.01	1.05	−8.9
	3.1	125	0.0291	210	−0.23	1.03	1.05	−9.9
	2.5	100	0.0296	174	0.35	1.04	1.04	−9.7

Table 1. Inflow properties of the LES experiments in this study. Simulations of the TNBL and CNBL use a surface roughness $z_0 = 10^{-4}$ m and Coriolis parameter $f_c = 1.03 \times 10^{-4}$ rad s^{-1}. In the CNBL, the Zilitinkevich number is $N/f_c = 55.5$, where N is the Brunt–Väisälä frequency.

increases with increasing relative Coriolis strength (decreasing Ro). However, wind direction profiles are increasingly nonlinear in the rotor area as the TNBL height decreases with decreasing Rossby number. The change in time-mean wind direction from the bottom to the top of the rotor is defined as $\Delta\psi = \psi(z_h + D/2) - \psi(z_h - D/2)$ for the time-averaged wind direction $\psi(z) = \arctan(\langle\bar{v}^B\rangle_{xy}/\langle\bar{u}^B\rangle_{xy})$. Note that profiles of $\bar{v}^B(z)$ look very similar to profiles of $\psi(z)$. Overall, due to the presence of the bottom boundary, the TNBL inflow is significantly more complex than the uniform inflow simulations.

In the CNBL, the boundary layer growth is suppressed relative to the TNBL due to the presence of the stable free atmosphere. The low-level jet is stronger in the CNBL than in the TNBL and the maximum wind speed reaches $1.05G$. The non-dimensional friction velocity in the CNBL decreases with increasing Rossby number, which is consistent with simulations from Liu *et al.* (2021). The buoyancy length scale $L_b = u_*/N$, where $N = \sqrt{g\Gamma/\theta_0}$ is the Brunt–Väisälä frequency, varies between 12.8 m at $Ro = 100$ and 100 m for $Ro = 1000$, which is larger than the vertical grid resolution $\Delta_z = 12$ m, allowing buoyancy effects to be resolved. Similar to the TNBL, there is a non-monotonic trend in the wind direction profiles across the turbine rotor $\Delta\psi$. That is, the change in wind direction across the rotor does not monotonically increase with increasing relative Coriolis forcing strength. Wind direction shear across the rotor of the turbine $\Delta\psi$ spans a larger range of values for the same parametric sweep of Ro in the CNBL than in the TNBL (see table 1).

Differences between the TNBL and CNBL development are a result of the stable free atmosphere in conventionally neutral conditions. Profiles of horizontally and time-averaged horizontal shear stress and buoyancy flux are shown in figure 4. The presence of negative buoyancy flux $\overline{w'\theta'}$, shown in figure 4(f), reduces shear stresses $\bar{\tau}_{xz} = \overline{u'w'} + \bar{\tau}^d_{13}$ and $\bar{\tau}_{yz} = \overline{v'w'} + \bar{\tau}^d_{23}$ in the CNBL. Therefore, the ABL height h is lower in the CNBL than in the TNBL for the same Rossby number, and the wind shear (speed and direction) in the CNBL is enhanced relative to the TNBL. A significant consequence of the negative

https://doi.org/10.1017/jfm.2025.35 Published online by Cambridge University Press

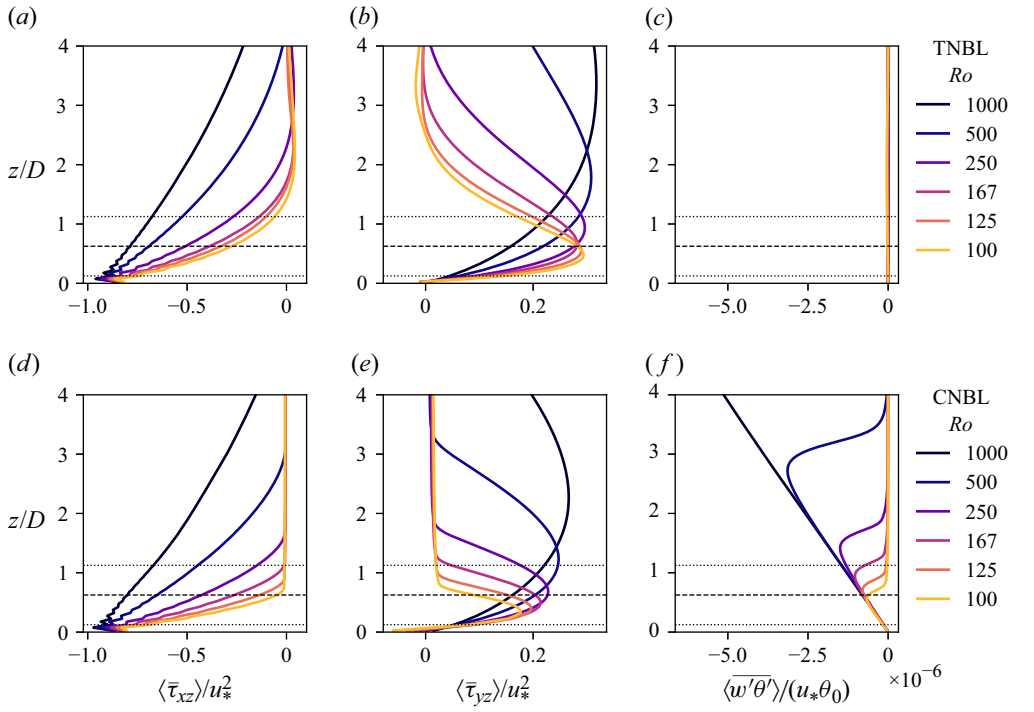

Figure 4. Profiles of horizontally and time-averaged fluxes in the (*a–c*) TNBL and (*d–f*) CNBL showing horizontal shear stress in the (*a*,*d*) streamwise and (*b*,*e*) lateral directions, normalised by the friction velocity u_*, as well as the (*c*, *f*) buoyancy flux.

buoyancy flux is in the low-Rossby-number simulations ($Ro \leq 167$), where the CNBL is sufficiently shallow that the turbine, which reaches up to 270 m at the rotor tip, impinges on the free atmosphere. As will be discussed in §§ 4.4 and 4.5, the interaction between the rotor and the free atmosphere induces gravity waves, which affect the wake dynamics.

4.2. *Qualitative time-averaged wake behaviour*

In this section, we examine the time-averaged wake velocity fields. Cross-sections of the hub height velocity deficit field $\overline{\Delta u_i} = \bar{u}_i - \langle \bar{u}_i^B \rangle_{xy}$ in the streamwise direction ($i = 1$) are shown in figure 5, where $\langle \bar{u}_i^B \rangle_{xy}$ is the horizontally and time-averaged precursor flow. The precursor flow is the base flow without wakes. In uniform inflow, wake recovery does not begin until very far downstream ($x/D \gtrsim 12$) due to the lack of free stream turbulence (Olivares-Espinosa *et al.* 2014; Howland *et al.* 2016). Wake deflection is anti-clockwise as viewed from above (deflection is in the $+y$ direction in the chosen coordinate system). The amount of wake deflection increases with increasing relative Coriolis forcing strength (i.e. decreasing Ro).

For the TNBL and CNBL inflows, wakes recover due to free stream turbulence. The wake recovery in all simulations is qualitatively only minimally affected by the parametric effects of Ro, despite the large variation in turbulence intensity, which is dependent on Ro, across the rotor plane. Wake deflection is also increasingly anti-clockwise as the relative strength of Coriolis forcing increases, which is particularly noticeable in the CNBL simulations at low Rossby numbers. A quantitative investigation of the wake dynamics in the ABL flows is given in §§ 4.4 and 4.5.

https://doi.org/10.1017/jfm.2025.35 Published online by Cambridge University Press

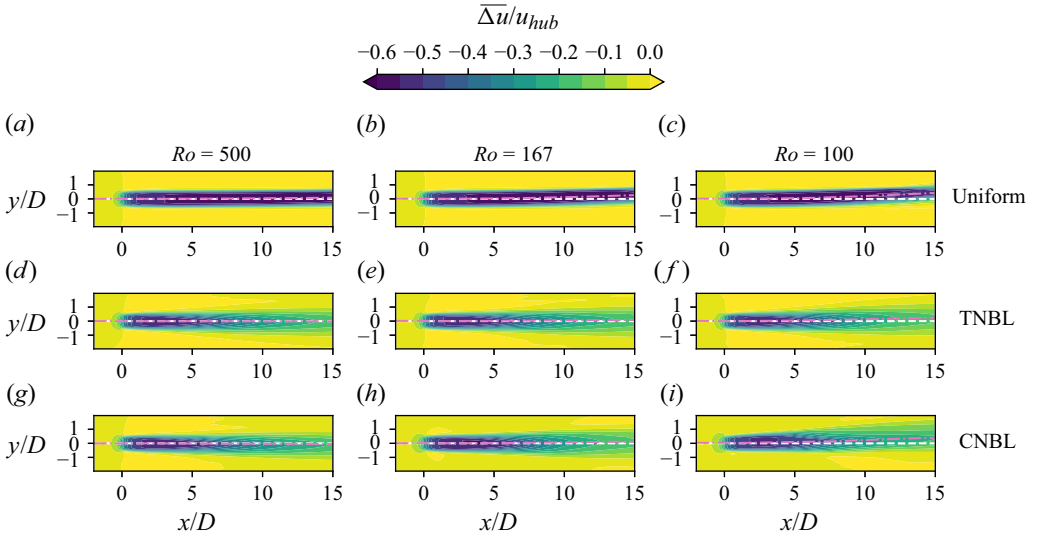

Figure 5. Hub height wind turbine wakes visualised as the streamwise velocity deficit with respect to the inflow, viewed from above, for varying Rossby numbers in (*a*,*b*,*c*) uniform inflow, (*d*,*e*,*f*) TNBL inflow and (*g*,*h*,*i*) CNBL inflow. The dashed white line indicates $y = 0$ while pink dash-dotted lines show the wake centreline.

Vertical slices through the yz-plane are shown in figure 6 at a distance $x = 8D$ downwind of the rotor. By $x = 8D$, variations in the relative Coriolis forcing strength can be observed in the uniform inflow wakes, with lower Rossby numbers deflecting farther in the $+y$ direction. In the TNBL, wakes are skewed, which is a result of the inflow wind direction shear (Magnusson & Smedman 1994; Abkar & Porté-Agel 2016). The difference in wake skewing between Rossby numbers is small, owing to the small spread in wind direction change over the rotor $\Delta\psi$ for the TNBL simulations.

In the CNBL, the decreasing boundary layer height as the Rossby number decreases strongly affects the wake shape. The large differences in wake shape between the CNBL simulations result from the changing inflow properties. Because the inflow wind direction is increasingly nonlinear with decreasing Ro, wake velocity slices assume complex shapes that are not well approximated by axisymmetric or elliptical (skewed) Gaussian wakes (Abkar & Porté-Agel 2016). Additionally, the wind speed shear across the rotor is increasingly complex as the ABL height decreases and the rotor interacts directly with the low-level jet. Finally, the ambient turbulence intensity varies substantially across the rotor, particularly for $Ro = 125$ and $Ro = 100$, which is distinct from the TNBL simulations.

4.3. *Uniform inflow results*

The uniform inflow simulations represent the canonical flow building block for understanding the dynamics of turbine wakes in the presence of Coriolis forces. Specifically, the uniform inflow environment separates Coriolis forcing from wind shear. Although the presence of uniform (i.e. gradient-free and non-turbulent) inflow cannot exist in the ABL due to the presence of the ground, it is helpful to study as a basis for parsing the leading-order dynamics governing wake structure and evolution in more complex inflows. The main limitation of the uniform inflow numerical set-up is the unphysical delay in the onset of a fully turbulent far wake, due to the absence of inflow wind shear or turbulence (Olivares-Espinosa *et al.* 2014; Howland *et al.* 2016), as shown in figure 5. Therefore, we will not attempt to draw conclusions from the streamwise momentum

https://doi.org/10.1017/jfm.2025.35 Published online by Cambridge University Press

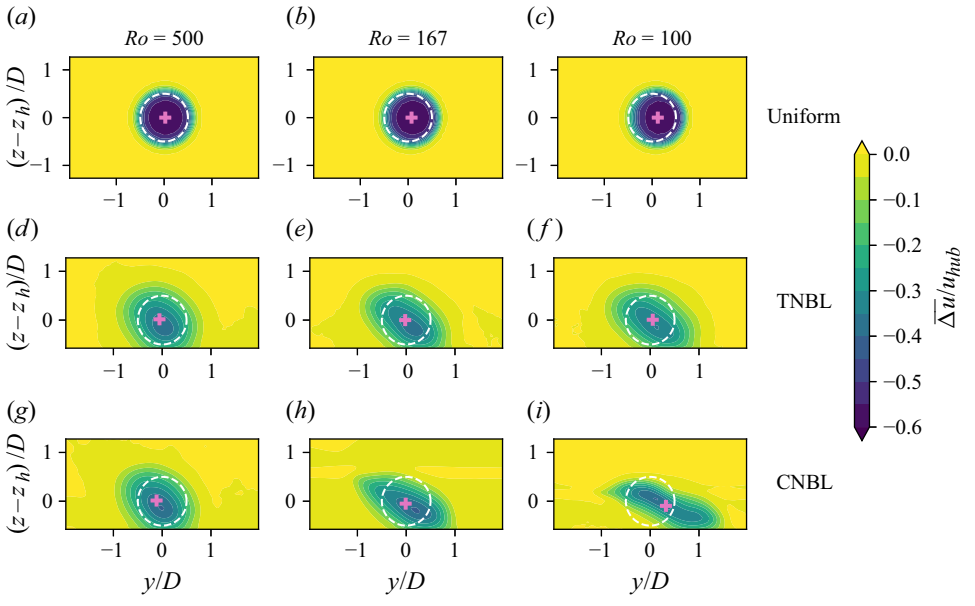

Figure 6. Wake cross-sections at $x/D = 8$ visualised as the streamwise velocity deficit with respect to the inflow for varying Rossby numbers in (a,b,c) uniform inflow, (d,e,f) TNBL inflow and (g,h,i) CNBL inflow. The turbine location is given by the white circle centred around the origin and the wake centroid position is given by the pink +.

budgets regarding wake recovery using the uniform inflow set-up. Nonetheless, we will show that the dynamics of the uniform inflow problem are complex and instructive for parsing mechanisms of lateral momentum transport which affect wake evolution in the presence of Coriolis forces.

We begin by investigating the wake deflection due to the Coriolis force in uniform inflow. Here, we choose to measure the wake deflection $y_c(x)$ as the centroid of the streamtube cross-section in the yz-plane. The wake deflection increases monotonically with increasing relative Coriolis forcing strength (decreasing Ro) and follows a parabolic trajectory, as shown in figure 7(a). By scaling the wake deflection y_c by the Rossby number, shown in figure 7(b), we see that the wake deflection collapses on to one curve until $x/D \approx 12$. The collapse worsens for $x/D > 12$ due to wake breakdown and turbulence. The collapse in the scaled wake deflection allows us to focus on understanding the wake dynamics at one Rossby number with the expectation that the relevant physical transport mechanisms will scale with the Rossby number.

The wake deflection is the integrated form of the lateral momentum budget. Therefore, in uniform inflow, the lateral momentum budgets should also collapse if scaled by the Rossby number. Individual terms M_y in the streamtube-averaged lateral momentum balance (3.3) are shown in figure 8 as a function of streamwise position downwind of the turbine. The individual terms, when scaled by the Rossby number, are of the order of unity and collapse together. All of the forcing terms are nearly constant in x outside of the wake expansion region $x/D \lesssim 1$ until wake recovery begins at $x/D \approx 12$. Therefore, the uniform inflow centroid position follows a parabolic trajectory due to constant acceleration (mean advection). When wake recovery begins, the wake velocity deficit $(G_1 - \bar{u})$ decreases, which decreases the strength of the Coriolis term and, by extension, the lateral advection of the wake. The Coriolis forcing term is the largest in magnitude and positive in sign (in the northern hemisphere), which results in a positive lateral acceleration and therefore a net

https://doi.org/10.1017/jfm.2025.35 Published online by Cambridge University Press

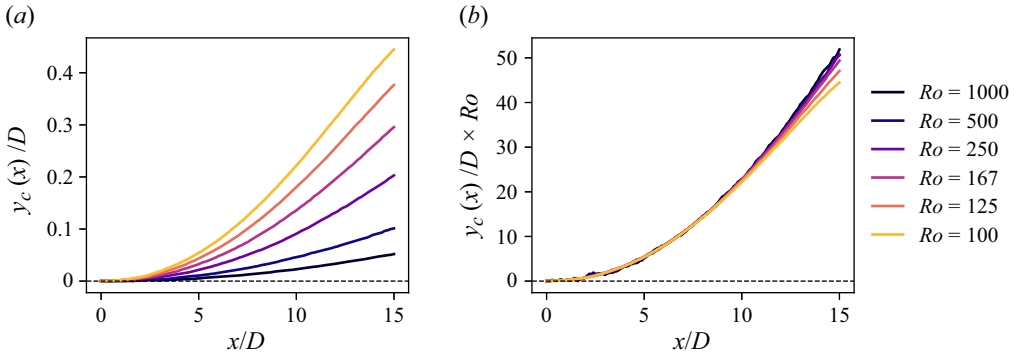

Figure 7. (*a*) Streamtube centroid position $y_c(x)$ as a function of downstream distance x in uniform inflow varying the Rossby number. (*b*) Scaling by the Rossby number collapses all uniform inflow simulations onto one curve.

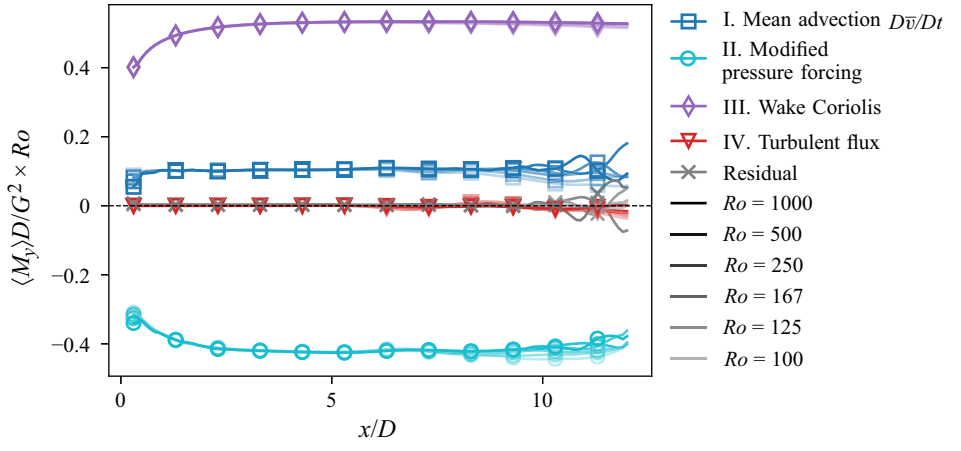

Figure 8. All terms in the lateral momentum balance for the uniform inflow simulations, streamtube-averaged and plotted as a function of streamwise distance. The streamtube-averaged quantities are scaled by the Rossby number Ro, showing similarity in the flow.

positive lateral advection of the wake region. However, the presence of a lateral pressure gradient opposes the direct Coriolis forcing term. The result of the pressure gradient is a net acceleration which is only approximately 25 % as strong as the direct Coriolis forcing term. Note that as the advection term is non-negligible, the wake flow is not in geostrophic balance.

We seek to investigate the physical mechanism that results in a non-zero lateral pressure gradient. The streamtube averaged lateral pressure gradient in the absence of Coriolis forcing is equal to zero. To investigate how Coriolis effects give rise to the lateral pressure gradients, we visualise streamlines of the in-plane velocity components $\bar{v}$, $\bar{w}$ at a cross-section $x/D = 10$ in figure 9(*a*). Streamlines of the in-plane velocity components at $Ro = 100$ show the presence of a counter-rotating vortex pair (CVP), which is the source of the wake deflection. The formation of the CVP, which is visualised by the formation of streamwise vorticity $\omega_1 = \omega_x$, can be understood through the vorticity budget equation. We take the curl of (3.1) to solve for the Reynolds-averaged vorticity equation. This

https://doi.org/10.1017/jfm.2025.35 Published online by Cambridge University Press

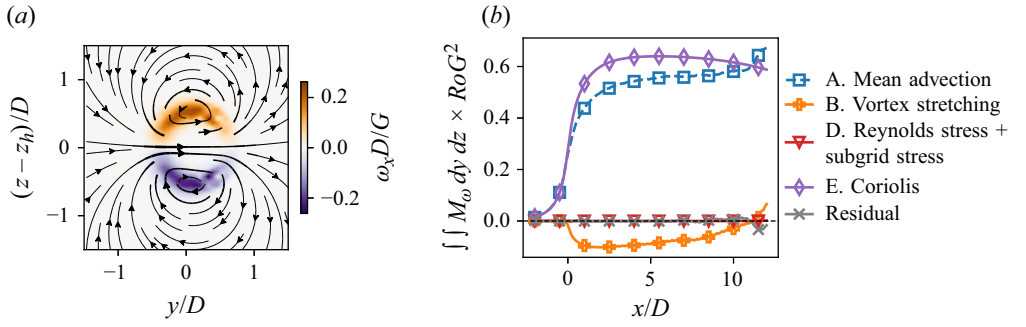

Figure 9. (*a*) Streamlines of in-plane velocities $\bar{v}$ and $\bar{w}$ at $Ro = 100$ and $x = 10D$. Contours of vorticity are superimposed, showing a counter-rotating vortex pair (CVP) with positive streamwise vorticity above the hub plane and negative vorticity below. (*b*) Streamwise vorticity budget terms M_ω scaled by Ro for the case $Ro = 100$, integrated for $z > z_h$. Streamwise vorticity advection (dashed blue) is balanced by Coriolis production (purple). Buoyancy torque (term C) is omitted as the uniform inflow simulations do not solve the potential temperature equation.

yields

$$\underbrace{\bar{u}_j \frac{\partial \bar{\omega}_i}{\partial x_j}}_{\text{A}} = \underbrace{\bar{\omega}_j \frac{\partial \bar{u}_i}{\partial x_j}}_{\text{B}} \underbrace{+ \frac{\varepsilon_{ij3}}{Fr^2 \theta_0} \frac{\partial \bar{\theta}}{\partial x_j}}_{\text{C}} \underbrace{- \varepsilon_{ijk} \frac{\partial}{\partial x_j} \left(\frac{\partial \bar{\tau}_{km}}{\partial x_m} + \frac{\partial \overline{u_k' u_m'}}{\partial x_m} \right)}_{\text{D}} \underbrace{+ \frac{1}{Ro} \frac{\partial \bar{u}_i}{\partial x_3}}_{\text{E}}, \tag{4.1}$$

where the bracketed terms are: (A) advection by the mean flow; (B) vortex stretching; (C) buoyancy torque; (D) torque from subgrid and Reynolds stresses and (E) Coriolis. The streamwise vorticity causes the CVP formation in uniform inflow. The integrated streamwise vorticity budget ($i = 1$) in figure 9(*b*) shows that the transfer of vorticity due to the Coriolis force is the largest contributor to the vorticity budget (4.1). The Coriolis term is primarily balanced by the mean advection of vorticity, where terms are again of order unity after being scaled by Ro. This balance can be written as

$$\bar{u}_j \frac{\partial \bar{\omega}_x}{\partial x_j} \approx \bar{u} \frac{\partial \bar{\omega}_x}{\partial x} \approx \frac{1}{Ro} \frac{\partial \bar{u}}{\partial z}. \tag{4.2}$$

In the vorticity balance, the role of the Coriolis force is to introduce planetary vorticity into the wake dynamics. The presence of the wake induces vertical velocity gradients ($\partial \bar{u}/\partial z$) such that positive streamwise vorticity is generated above hub height (in the northern hemisphere), and *vice versa* below hub height.

Lateral velocities induced by a CVP are also the mechanism for wake deflection in yaw-misaligned turbines (Howland *et al.* 2016; Bastankhah & Porté-Agel 2016). Wakes trailing yawed turbines are a widely studied case in recent literature (Meyers *et al.* 2022), and therefore, we make an analogy between the flow physics from Coriolis effects and yawed turbine wakes here. Traditionally, modelling the deflection of yaw-misaligned wind turbine wakes with momentum-based approaches has yielded overpredictions of the wake deflection because the lateral pressure gradient forces on the streamtube, which are non-negligible, are neglected for model simplicity (Jiménez *et al.* 2010; Shapiro *et al.* 2018; Heck *et al.* 2023). For wakes in uniform inflow with Coriolis forcing, the presence of a CVP also induces a non-negligible lateral pressure gradient force. The role of the pressure gradient forcing, as is the case in yaw-misaligned wind turbine wakes, is to enforce mass conservation (Bastankhah & Porté-Agel 2016). Neglecting the pressure gradient forcing in (3.3) leads to an order-of-magnitude overprediction in the wake deflection (not shown).

https://doi.org/10.1017/jfm.2025.35 Published online by Cambridge University Press

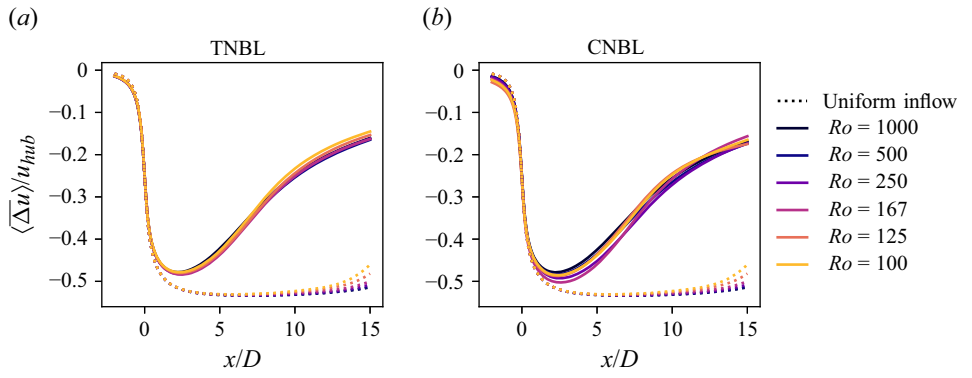

Figure 10. Streamtube-averaged streamwise velocity deficit as a function of streamwise coordinate x/D in (*a*) TNBL inflow and (*b*) CNBL inflow. Uniform inflow wakes are shown with dotted lines.

In summary, the net effect of the Coriolis force on wakes in uniform inflow is an anti-clockwise deflection that increases with increasing relative Coriolis forcing strength. In the lateral momentum budget, the Coriolis term is the largest in magnitude but partially cancelled by a lateral pressure gradient force in the wake. Wake deflection is caused by the formation of a CVP due to the transfer of planetary vorticity into the streamwise direction via the wake-added shear. The CVP is responsible for creating $\bar{v} > 0$ inside the wake (in the northern hemisphere), which deflects the wake anti-clockwise and gives rise to the non-negligible lateral pressure gradient force. Neglecting the pressure gradient forcing in a momentum-based modelling approach results in an overprediction in the wake deflection.

4.4. *Coriolis effects on streamwise momentum in the ABL*

This section focuses on wake recovery in TNBL and CNBL conditions. The streamtube-averaged streamwise velocity deficit is shown as a function of streamwise distance in figure 10. In the uniform inflow cases, shown as dotted lines in figure 10, the streamtube-averaged velocity deficit is constant after the pressure recovery in the near-wake of the turbine. Additionally, the uniform inflow wake recovery does not depend on the strength of Coriolis forcing. Overall, in uniform inflow, we observe very weak parametric dependence of relative Coriolis forcing strength on wake recovery.

In the TNBL, the relative strength of Coriolis forcing weakly affects the wake recovery. Due to wind shear in the ABL inflow, the turbine thrust in the TNBL is lower than in uniform inflow. As a result, the wake velocity deficit magnitude is lower in the TNBL than in uniform inflow. In the far wake, the strongest relative Coriolis forcing experiences the fastest wake recovery, and the wake recovery rate generally decreases as Ro increases. We emphasise that the relative differences in wake strength between Rossby numbers are modest, and we further elaborate on the statistical significance of the differences in wake recovery for varying Ro in § 4.6.

Trends in wake velocity as a function of Ro are less clear in the CNBL. This is due to the suppressed ABL height, which results in complex inflow conditions across the rotor area, as noted in § 4.2. For example, the wind speed profile changes significantly as the boundary layer height decreases and the low-level jet interacts with the rotor. This affects the rotor thrust, which increases monotonically with decreasing CNBL height. As a result, the maximum velocity deficit, which occurs around $x \approx 2.5D$, changes in magnitude with the Rossby number. Further, the turbulence intensity also varies more in the CNBL than in the TNBL as a function of the Rossby number. In contrast with the TNBL wakes, wake

https://doi.org/10.1017/jfm.2025.35 Published online by Cambridge University Press

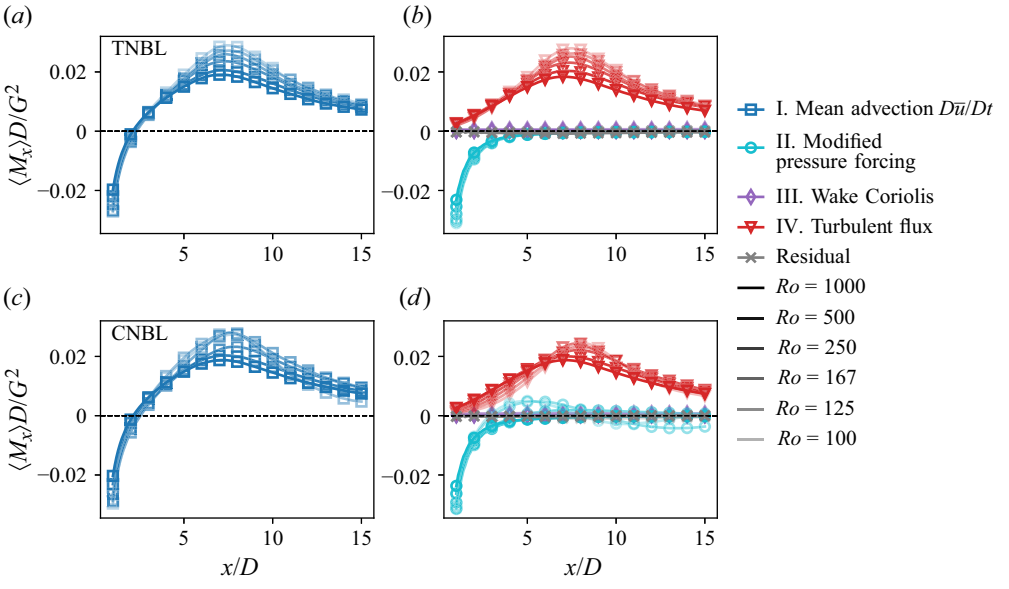

Figure 11. Streamtube-averaged streamwise momentum budget terms M_x for wakes in the (a,b) TNBL and (c,d) CNBL. The mean advection is the sum of all forcing terms.

recovery rates in the CNBL do not follow a clear trend with changing Rossby numbers. To parse the dynamics of the wake recovery, we analyse the streamwise momentum budget in the wake.

Wake recovery is described by the streamwise momentum budget. The streamtube-averaged streamwise momentum budget is shown in figure 11 for wakes in the TNBL and CNBL. For $x \lesssim 3D$, the modified pressure forcing is large due to the pressure recovery from the forcing at the rotor. Beyond this region, turbulent fluxes (divergence of Reynolds stresses) replenish momentum into the wake, comprising the leading-order dynamics.

In the TNBL, the wake recovery due to the turbulent flux of momentum accounts for nearly all (95 %–99 %) of the wake recovery. Effects of direct Coriolis forcing, subgrid stresses and pressure gradients are negligible in the streamwise momentum budget. In other words, the dependence of the streamwise momentum budget on relative Coriolis forcing strength is primarily through changes in the ABL structure, which depends on the Rossby number (see figure 3). The Reynolds stress divergence in the wake, and therefore wake recovery rate, increases as the relative strength of Coriolis forcing increases. For all Rossby numbers, the Reynolds stress divergence reaches a maximum value near $x = 8D$. The marginal increase in wake recovery rate with decreasing Rossby number shown in figure 10(a) is enabled by the increasing turbulent flux in the wake.

We observe two notable differences between the TNBL and CNBL streamwise momentum budgets. One notable difference is that the pressure gradient force deviates from the asymptotic recovery expected from classical momentum theory for $Ro \leq 167$. Instead, oscillations are observed in the pressure gradient term. These oscillations stem from gravity waves induced by the free-standing turbine, which interact directly with the capping inversion when $z_{tip} \gtrsim h$, where $z_{tip} = z_h + 0.5D$ is the rotor tip height. Gravity wave excitation from large wind farms has been studied extensively in recent literature (e.g. Allaerts & Meyers 2017; Sanchez Gomez *et al.* 2023; Lanzilao & Meyers 2024). The presence of the turbine perturbs the capping inversion upward, exciting gravity waves that non-locally redistribute kinetic energy through pressure oscillations. While gravity

https://doi.org/10.1017/jfm.2025.35 Published online by Cambridge University Press

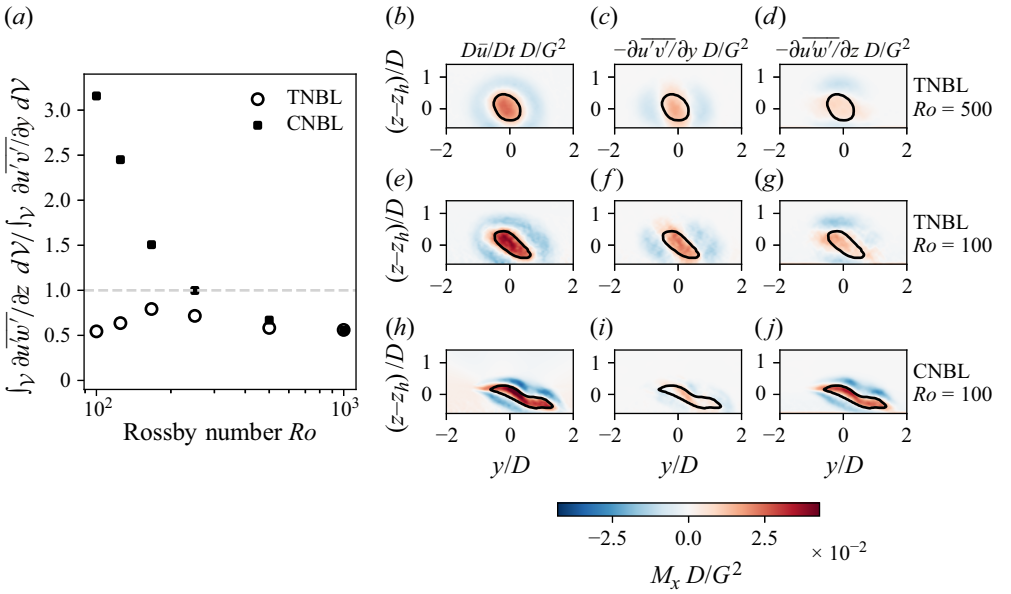

Figure 12. (*a*) Ratio of vertical to lateral turbulent momentum flux into the wake streamtube. (*b–j*) Profiles in the yz-plane at $x = 8D$ of gradients of turbulent momentum flux, where reds indicate acceleration (wake recovery) and blues indicate deceleration. The streamtube boundary is outlined in black.

waves are not the main focus of this study, the pressure gradient forcing due to gravity waves is dynamically significant to the streamwise and lateral momentum budgets (see § 4.5). Sensitivity tests at low Rossby numbers with a doubled vertical domain height L_z and adjusted RDL strength show that our numerical set-up does not significantly affect the wake dynamics or results (see figure 20 in Appendix A.5). We suggest future work investigating the interactions between the rotor, wakes and the free atmosphere. Finally, we note that because gravity wave effects are inherently non-local, additional surrounding turbines may change the development of gravity waves and should be studied separately.

A second notable difference between the TNBL and CNBL streamwise momentum budgets is that the inflow turbulence intensity at the rotor hub height increases more with increasing Ro in the CNBL than in the TNBL. As a result, the turbulence flux term in figure 10(*d*) monotonically increases with increasing Rossby number for $x \lesssim 5D$. The peak Reynolds stress divergence still generally increases with increasing relative Coriolis forcing (decreasing Ro), as was observed in the TNBL. The exception is for the cases where stable thermal stratification in the free atmosphere suppresses turbulence and therefore wake recovery due to the shallow CNBL height ($Ro = 125$ and $Ro = 100$).

To examine the parametric dependence of the turbulent momentum flux on the Rossby number, we take a further look at the Reynolds stress divergence term. In figure 12, we break out the wake recovery due to the Reynolds stress divergence into lateral ($M_{x,2}$) and vertical ($M_{x,3}$) turbulent momentum fluxes. The streamwise Reynolds stress component is not shown because it is small compared with the in-plane components and integrates to nearly zero inside the streamtube for $x \in [0, 15]D$.

Both the magnitude and structure of turbulent fluxes change as a function of Ro. In figure 12(*a*), the ratio of vertical to lateral turbulent momentum flux $M_{x,3}/M_{x,2}$, integrated over the entire streamtube from the rotor to $x = 15D$, are shown as a function of Ro. In the present simulations of a single turbine wake in the TNBL, the vertical momentum flux contribution is between 55 % and 80 % of the lateral momentum flux contribution to the

https://doi.org/10.1017/jfm.2025.35 Published online by Cambridge University Press

wake recovery. While the ratio of vertical to lateral momentum flux changes modestly with Ro in the TNBL, the dependence of $M_{x,3}/M_{x,2}$ on Ro in the CNBL is more pronounced. In the CNBL, as the relative Coriolis forcing strength increases and ABL height decreases, wake recovery is increasingly driven by vertical momentum fluxes. We note that while the ratio of turbulent fluxes is dependent on ABL properties and Rossby number, as shown here, it is also dependent on lateral turbine spacing if neighbouring turbines are present (Calaf *et al.* 2010; van der Laan *et al.* 2023). Therefore, the dependence of wake recovery on Rossby number may differ for turbine wakes in wind farms compared with the wakes of free-standing turbines studied here.

We visualise turbulent momentum flux contributions to the wake recovery in figure 12(*b–j*). Contours of the mean streamwise advection, lateral Reynolds stress gradient and vertical Reynolds stress gradient are shown in a yz-plane at a distance $x = 8D$ downwind for three atmospheric conditions. In all cases, the streamtube boundary corresponds closely to the boundary between net Reynolds stress convergence (acceleration) and divergence (deceleration). That is, the streamtube-averaged quantities robustly select the wake region which is accelerating and recovering lost momentum. At $Ro = 500$, the TNBL and CNBL wake recovery is very similar, as shown by figure 12(*a*), so only the contours of the TNBL wake are shown. Between $Ro = 500$ and $Ro = 100$ in the TNBL and CNBL, the magnitude of the mean advection within the streamtube increases. In the TNBL, changes in the Rossby number only weakly affect the wake shape and the ABL structure, so the individual turbulent flux contributions are similar between $Ro = 100$ and $Ro = 500$. In the CNBL, wakes experience strong wind direction shear as the ABL height decreases with decreasing Ro. This strongly skews the wake and causes more vertical momentum entrainment than lateral entrainment of streamwise momentum. To summarise, while differences in overall wake recovery are small between Rossby numbers, wake recovery mechanisms change substantially as the ABL height decreases.

4.5. *Coriolis effects on lateral momentum*

As noted in the introduction, there are two distinct coupled effects from Coriolis forces that alter the structure of wakes in the ABL. First, the wake skews due to wind direction shear, where different vertical levels z are subjected to different inflow wind angles. This skewed wake is visualised in figure 6(*d–i*), and the effect has been explored in previous literature (Abkar & Porté-Agel 2016; Churchfield & Sirnivas 2018) and modelled with wake modelling approaches (Abkar *et al.* 2018; Martínez-Tossas *et al.* 2021). In addition to the lateral wake advection induced by Coriolis forces through wind direction shear, Coriolis forces also affect wake dynamics, primarily through lateral momentum equations. Wake deflection is caused by an imbalance of lateral forcing terms in the wake as a whole. Previous literature has mostly explored the advective mechanisms that cause wake skewing. In contrast, we focus on Coriolis effects on wake dynamics, which primarily affect lateral deflection of the wake. The extent to which wake skewing or wake deflection are significant to farm design will depend on the layout, control strategy and ABL conditions of a wind farm. Future work should compare these different effects in a case study.

Wake deflection, which is shown in figure 5, is influenced by the relative strength of Coriolis forces. Here, we measure the wake deflection by computing the centroid of the streamtube position, consistent with the analysis in § 4.3. The wake centroid evolution $y_c(x)$ is shown in figure 13(*a*,*b*) for varying Rossby numbers with each inflow type. Because the hub height wind direction oscillates after the wind angle controller is turned off at the beginning of the concurrent simulations, the wind direction drifts up to 1°

https://doi.org/10.1017/jfm.2025.35 Published online by Cambridge University Press

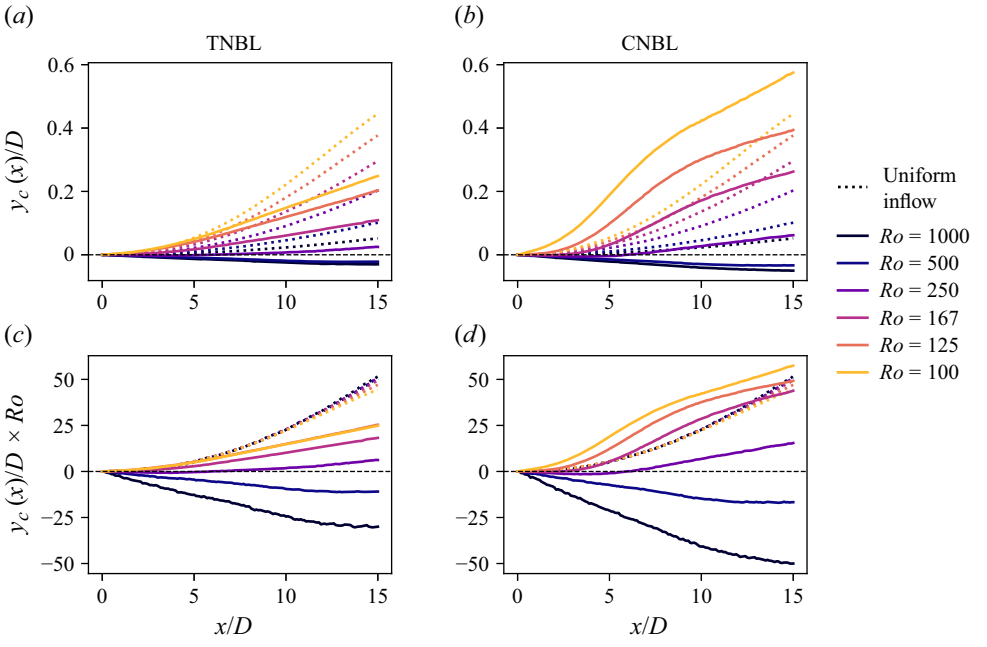

Figure 13. (*a*,*b*) Wake centroid location, defined as the centroid of the streamtube, as a function of streamwise coordinate x/D for varying Rossby numbers in the (*a*) TNBL and (*b*) CNBL. (*c*,*d*) Wake deflections are scaled by the Rossby number. Uniform inflow wake deflections are overlaid with the dotted lines.

throughout the averaging time of the primary simulation. The advection due to the time-mean wind direction at hub height is removed by subtracting $x\tan(\psi_{hub}) \approx \psi_{hub}x$ from the streamtube centroid $y_c(x)$, where ψ_{hub} is given in table 1.

In all inflow conditions (uniform, TNBL and CNBL), the amount of wake deflection is parametrically dependent on the relative strength of Coriolis forcing. The sign (clockwise or anti-clockwise) of the wake deflection is also dependent on the relative strength of Coriolis forcing for wakes in the ABL. This differs from the uniform inflow cases, which only deflect anti-clockwise in the northern hemisphere. Note that as clockwise and anti-clockwise deflections are observed in ABL inflow conditions, the wake deflection does not collapse when scaled by the Rossby number, as shown in figure 13(*c*,*d*). Between $Ro = 500$ and $Ro = 250$, we observe a transition in wake deflection direction in the ABL. For $Ro = 500$, wakes in ABL inflow are deflected clockwise as viewed from above ($-y$ direction), while for $Ro \leq 250$, wakes are deflected anti-clockwise ($+y$ direction). While the wake deflection will depend on ABL conditions, including surface roughness, subsidence, orography, etc., we expect that the qualitative trends presented here will apply to other neutral ABLs, even if no universal transitional Rossby number applies to all neutral ABLs. Finally, the wake deflection is not bounded above or below by the uniform inflow results. For example, in the CNBL at $Ro = 100$, the observed wake deflection is several times larger than the wake deflection in uniform inflow for $x/D \lesssim 6$.

To understand why wakes are deflected increasingly anti-clockwise with decreasing Rossby number (increasing relative Coriolis forcing strength), we examine the lateral momentum budget terms M_y averaged within the streamtube, shown in figure 14. Recall that in the absence of planetary rotation (i.e. $Ro \to \infty$), the wake is symmetric across the y-axis, and the streamtube-averaged momentum budget averages to zero. With the introduction of Coriolis forces at finite Rossby numbers, which break this symmetry,

https://doi.org/10.1017/jfm.2025.35 Published online by Cambridge University Press

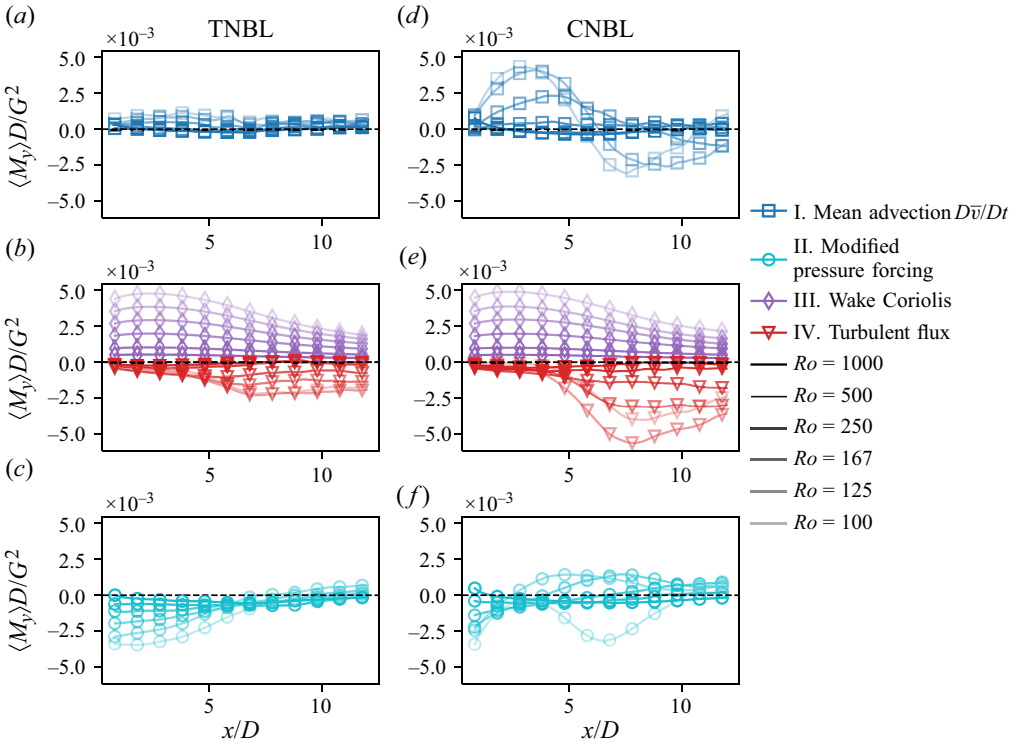

Figure 14. Streamtube-averaged momentum terms in the y-momentum balance for wakes in (a,b,c) TNBL inflow and (d,e,f) CNBL inflow.

terms in the lateral momentum budget become non-zero. The wake Coriolis forcing scales directly with Ro^{-1} and is large in magnitude compared with the other terms in the lateral momentum balance. This is in contrast to the streamwise momentum (§ 4.4) where the turbulent flux constitutes the largest forcing term and the direct Coriolis forcing term is negligible.

In the TNBL, the mean advection term is of the same order of magnitude as in uniform inflow. The mean advection of the streamtube is increasingly positive as the Rossby number decreases. Because the wake deflection is the integrated form of the mean lateral advection, the increasingly positive advection term results in increasingly anti-clockwise wake deflection. The mean advection is the sum of the wake Coriolis, modified pressure forcing and turbulent flux forcing terms (subgrid forcing is negligible). As shown in figure 14(a–c), the Coriolis, pressure gradient and Reynolds stress terms are all dynamically active in the wake, but the relative importance of each term varies with streamwise location x.

The wake Coriolis term is larger in magnitude than all other lateral forcing terms in the near-wake region. Similar to the uniform inflow simulations, the direct Coriolis forcing is again partially opposed by a lateral pressure gradient force. However, unlike in uniform inflow, the pressure gradient forcing term begins to decay almost immediately after the initial wake expansion. The decay of lateral pressure gradients in the TNBL occurs in conjunction with the lack of a coherent CVP formation in the TNBL turbine wake. A coherent CVP is not formed in the TNBL, as shown in the colour contours of figure 15(c), due to atmospheric turbulence. The lateral pressure gradients associated with

https://doi.org/10.1017/jfm.2025.35 Published online by Cambridge University Press

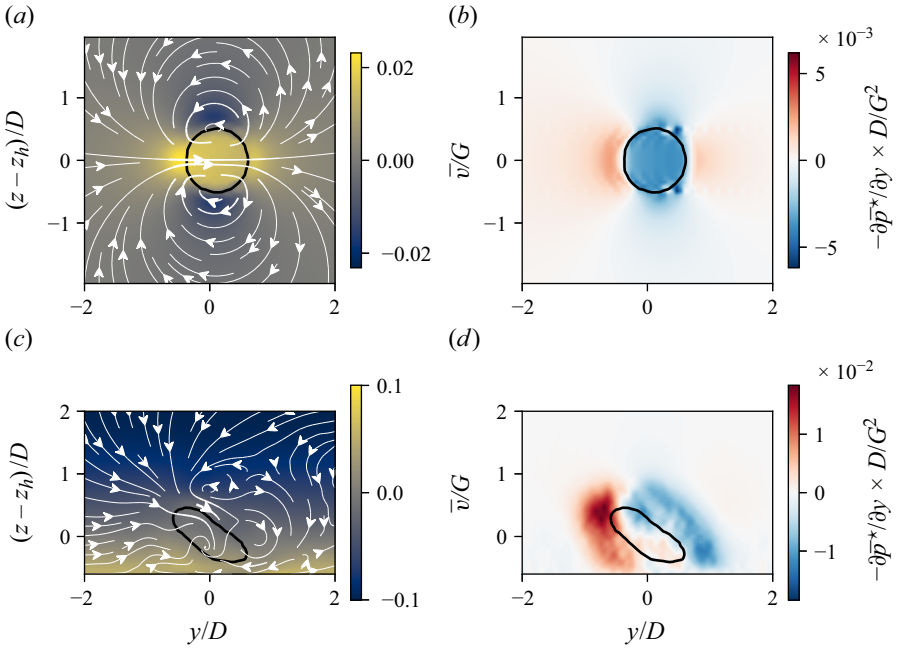

Figure 15. Wake cross-sections at $x = 8D$ for (*a*,*b*) uniform inflow and (*c*,*d*) TNBL simulations at $Ro = 100$. (*a*,*c*) Contours of lateral velocity $\bar{v}$ are shown with streamlines of $\overline{\Delta v}$ and $\overline{\Delta w}$ overlaid. (*b*,*d*) Lateral pressure gradient fields in the wake. Note the different colourbar magnitudes. The streamtube boundary is shown by the black line.

the CVP formation in uniform inflow are obscured by turbulence in the TNBL wake. The lateral pressure gradient field primarily opposes the Reynolds stress divergence, similar to pressure gradients in turbulent jet flows (Pope 2000). The asymmetry in the pressure gradient forcing in figure 15(*d*) is due to the Coriolis force. We note that a weak CVP can be observed in streamlines of the velocity deficit $\overline{\Delta v}$, $\overline{\Delta w}$ in the TNBL wake, seen in figure 15(*c*). Even so, the structure of the full lateral velocity field $\bar{v}$, shown by the colour contours, and pressure gradient field indicate that the effect of the CVP formation does not constitute the primary mechanism of momentum transport.

As the wake recovers, the direct Coriolis forcing term, which is proportional to the velocity deficit, begins to diminish. At the same time, the turbulent entrainment of lateral momentum increases. In the TNBL, we observe that the pressure gradient term responds to the combined Coriolis and pressure gradient forcing. For instance, the pressure gradient forcing flips sign in the wake region when the Reynolds stress divergence exceeds the direct Coriolis forcing. As a result, even in the far wake when the wake begins to recover and the direct Coriolis forcing decays, the wake continues to deflect in the TNBL, as quantified in figure 13. In contrast with the uniform inflow wakes, where the CVP formation drives the lateral pressure gradient forcing, turbulence primarily controls the lateral pressure gradient for wakes in the TNBL.

Comparing the TNBL and CNBL simulations in figure 14, we see both similarities and differences in the lateral momentum budgets. For example, the direct Coriolis forcing term, which depends only on wake velocity and Rossby number, is nearly the same in the TNBL and CNBL. This is because the streamtube-averaged wake velocity is very similar between the TNBL and CNBL for all Ro, as shown in figure 10. However, the magnitude of the turbulent flux of lateral momentum into the wake is greater in the CNBL

https://doi.org/10.1017/jfm.2025.35 Published online by Cambridge University Press

than in the TNBL, in general. The lateral momentum flux in the CNBL is generally larger than in the TNBL because the magnitude of wind direction shear is larger in the CNBL than in the TNBL for the same Rossby number. The most substantial difference between the TNBL and CNBL lateral momentum budgets is the presence of oscillations in the lateral pressure gradients with wavelengths of several turbine diameters or greater, shown in figure 14(f). As mentioned in § 4.4, the pressure oscillations are induced by gravity waves from the turbine interacting directly with the capping inversion. The wavelength of the oscillations decreases as the geostrophic wind speed decreases, as predicted by linear wave theory ($\lambda_x = 2\pi G_x/N$). Where waves are present ($Ro \lesssim 167$), oscillations due to gravity waves influence the pressure field and therefore the lateral pressure gradient forcing term. In the $Ro = 100$ and $Ro = 125$ simulations, the lateral pressure gradient decays rapidly in the near wake, which drastically increases the net lateral advection and therefore wake deflection in the CNBL inflow compared with the TNBL or uniform inflow. While the dynamics differ between the TNBL and CNBL due to free atmosphere stratification, we emphasise that the qualitative trends in wake deflection (figure 13) are the same: we observe parametrically varying wake deflection which can be clockwise or anti-clockwise, but is increasingly anti-clockwise as relative Coriolis forcing strength increases (Rossby number decreases).

The parametric dependence of the lateral momentum budget terms on the Rossby number has a direct connection to the wake deflection. In particular, because the momentum budget terms represent a forcing (and therefore acceleration) on the flow, integrating the lateral momentum budgets twice in time first yields lateral velocity, then wake deflection. Additionally, using the streamtube-averaged velocity $\langle \bar{u} \rangle$ to advect the flow, time integration can be transformed into spatial integration in the streamwise direction x. A mathematical derivation including the assumptions and transformations that connect the wake deflection to the forcing terms $\bar{f}_y$ in the lateral RANS budget (terms II–V in (3.3)) are given in Appendix D. The final result is

$$y_c(x) = \sum \underbrace{\int_{x_0}^{x} \frac{1}{\langle \bar{u} \rangle (x')} \int_{x_0}^{x'} \frac{1}{\langle \bar{u} \rangle (x'')} \langle \bar{f}_y(x'', y, z) \rangle \, \mathrm{d}x'' \, \mathrm{d}x'}_{\text{Individual forcing contributions}} + \underbrace{\int_{x_0}^{x} \frac{\langle \bar{v} \rangle (x_0)}{\langle \bar{u} \rangle (x')} \, \mathrm{d}x'}_{\text{Base Advection}} . \quad (4.3)$$

As a result of the integration, the observed streamtube deflection (figure 13) can be reconstructed from the streamtube-averaged momentum budgets, as shown in figure 16(a–b). Overall, the integrated budgets reconstruct the observed streamtube lateral deflection well, quantitatively capturing the streamtube deflection amount.

To extend this analysis, we represent the integrated contribution of each lateral forcing term as an equivalent wake deflection amount at $x = 10D$, shown in figure 16(c). Some forces, such as direct Coriolis forcing, cause anti-clockwise ($+y$ direction) wake deflection in the northern hemisphere. Other forces, such as the turbulent flux of lateral momentum, deflect wakes clockwise. Importantly, the turbulent flux of lateral momentum does not increase in magnitude as fast as the direct Coriolis forcing, resulting in increasingly anti-clockwise wake deflections with decreasing Ro. The lateral pressure gradient force generally opposes the Coriolis force, although in the CNBL, the integrated magnitude of the pressure gradients is strongly affected by gravity waves. For example, at $Ro = 125$ with the integration bounds $x \in [0, 10]D$, the pressure gradient contribution to the wake deflection is nearly zero (see figure 14f). While the net deflection and direct Coriolis forcing contribution monotonically increase with increasing relative Coriolis forcing

https://doi.org/10.1017/jfm.2025.35 Published online by Cambridge University Press

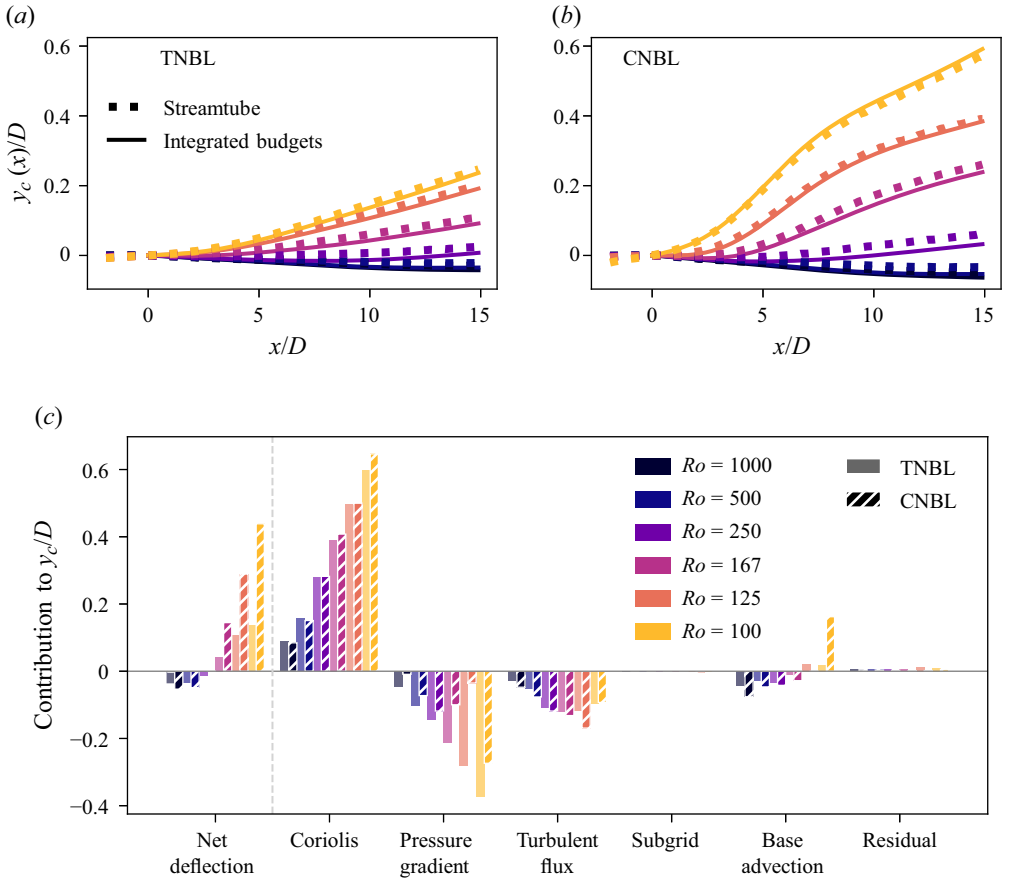

Figure 16. Integrated form of the lateral momentum budgets to reconstruct the streamtube centroid deflection in (*a*) TNBL inflow and (*b*) CNBL inflow. (*c*) Integrated contributions to the net streamtube deflection for each lateral forcing term at $x = 10D$. The net deflection, $y_c(x = 10D)$, is equal to the sum of deflection contributions from all forcing terms to the right of the vertical dashed line. The linear advection $x\psi_{hub}$ is subtracted from the net deflection and base advection columns.

(decreasing Ro), some forces, such as the lateral pressure gradients and turbulent fluxes, vary non-monotonically as a result of structural changes in the ABL with decreasing Ro such as decreasing inflow TI. Finally, the base advection term represents the nonlinear interaction between the non-zero lateral velocity at the rotor, which is due to the wind direction drift in the ABL and to Coriolis effects in the induction region of the wind turbine (Gadde & Stevens 2019), with the wake velocity deficit. As figure 16(*c*) shows, multiple lateral forcing terms have a leading-order importance on the wake deflection of a wake in the ABL, and each forcing term has a different parametric dependence on the relative strength of Coriolis forcing.

The integrated lateral momentum budgets link the momentum equations with the observed wake deflections. Due to the transformation from time coordinates to spatial coordinates through the streamwise velocity $\langle\bar{u}(x)\rangle$, the lateral forcing (acceleration) that occurs in the near-wake has a stronger effect on the wake deflection than forcing in the far-wake. This is because the wake velocity in the near-wake region is slower than in the far-wake and, therefore, the residence time of the near-wake is longer than in the far-wake. Notably, the largest lateral forcing term in the near-wake region is the

https://doi.org/10.1017/jfm.2025.35 Published online by Cambridge University Press

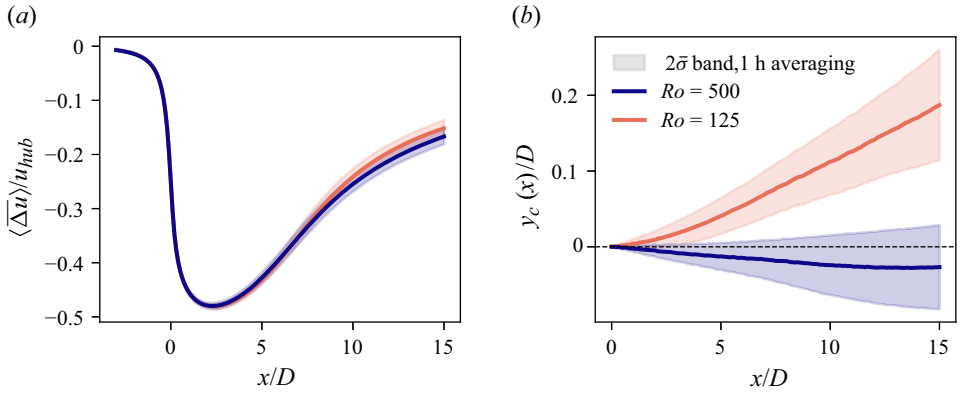

Figure 17. Variation in (*a*) wake recovery and (*b*) wake deflection for two Rossby numbers in TNBL inflow, showing a distribution from one-hour time-averaged flow fields.

anti-clockwise Coriolis forcing, shown in figure 14. Assuming a linearised advection velocity, $\langle\bar{u}(x)\rangle \approx u_{hub}$ fails to reconstruct the wake deflection from integrating the momentum budget and persistently underpredicts the wake deflection due to Coriolis effects. In summary, through a streamtube-averaged analysis of the wake momentum budget, we parse the importance of each ABL forcing term on the net wake deflection to explain the parametric variation of wake deflection on relative Coriolis forcing strength.

4.6. *Contextualising Coriolis-driven wake deflection with wind farm flow control*

Atmospheric conditions typically change on time scales of $\mathcal{O}(1\,\mathrm{h})$ (Stull 1988). A time averaging period of one inertial period $2\pi/f_c$ is used in the ABL simulations presented in this study to ensure that the reported dynamics is not affected by a partial period of an inertial oscillation. This time averaging period is much longer than the response time of the ABL. In other words, the ABL is rarely quasi-stationary for a whole inertial oscillation period. In this section, we compare the variation across Rossby numbers to the inherent variation in turbulence over one-hour averages.

To assign an interval of uncertainty to the reported wake statistics, we compare the full time average over one inertial period with non-overlapping one-hour time averages. The standard deviation of the mean $\bar{\sigma}$ is computed from the standard deviation of the ensemble of one-hour averages. A $2\bar{\sigma}$ band around the sample mean wake deflection and wake recovery is shown in figure 17 for two Rossby numbers in TNBL inflow. The advection from the base flow $x\psi_{hub}$ for each 1-hour average is subtracted from the wake deflection, like in figure 13, to focus on the variation in wake dynamics rather than on the variation in wind direction due to inertial oscillations. The Rossby numbers $Ro = 125$ and $Ro = 500$ approximately correspond with the cut-in and rated wind speed for the IEA 15-MW reference turbine.

The one-hour time-averaged metrics highlight the variability of mean winds and turbulence in the ABL within an inertial oscillation. For the streamwise velocity deficit shown in figure 17(*a*), the intervals between the two Rossby number values overlap. This indicates that the variability in wake recovery due to stochastic turbulence in the TNBL is greater than the variability in wake recovery due to Coriolis effects. That is, for the range of Rossby numbers studied here, we find no statistically significant impact of Coriolis effects on wake recovery of a free-standing turbine, relative to the internal variability of the ABL, for time scales relevant to the ABL or wind turbine control.

https://doi.org/10.1017/jfm.2025.35 Published online by Cambridge University Press

In contrast, the impact of relative Coriolis forcing strength on wake deflection is statistically significant, as shown in figure 17(*b*). For the Rossby number values relevant to the IEA 15-MW reference turbine, the difference in wake deflection due to Coriolis forcing exceeds the variance due to ABL turbulence over one-hour time scales. Additionally, the difference in wake deflection between Rossby numbers increases with increasing distance downwind. It is also interesting to note that for relatively weak Coriolis forcing ($Ro = 500$), the $2\bar{\sigma}$ envelope of variability includes zero and anti-clockwise wake deflections. Previous literature has focused on shorter time averaging lengths than presented here. Alongside variation in the ABL conditions, the spread of reported wake deflection may be partially attributed to variability of ABL turbulence over relatively short time scales.

Wake steering, or the intentional deflection of wind turbine wakes induced through yaw-misalignment of the rotor, has garnered attention as one way to increase collective power production of wind turbine arrays (Fleming *et al.* 2019; Howland *et al.* 2022). Previous work has focused on the combined effects of Coriolis forcing and wake steering, which both can act to deflect wakes in the ABL. In LES of a five-turbine array at $Ro = 1005$, Nouri *et al.* (2020) used wake steering to increase aggregate farm power production. They found that power production gains for positive yaw-misalignment angles increased over negative yaw misalignments when Coriolis forces were present in the inflow (Nouri *et al.* 2020). Here, positive yaw misalignments are anti-clockwise turbine rotations about the vertical axis, which induce clockwise wake deflection. Similarly, Wei *et al.* (2023) recommend positive yaw misalignments for fully waked conditions in the northern hemisphere.

While we focus on wakes of yaw-aligned turbines in this study, we can quantify the magnitude of equivalent yaw misalignment which would equal the wake deflection observed due to Coriolis forcing alone. To predict the wake deflection due to yaw misalignment, we use the model proposed by Shapiro *et al.* (2018) and extended by Heck *et al.* (2023) using a wake spreading rate of $k_w = 0.083$ and the same turbine thrust coefficient $C_T' = 1.33$. We find that for $Ro = 125$, the equivalent yaw misalignment for the observed wake deflection at $x = 10D$ in the TNBL is approximately $-13°$, while in the CNBL, it is approximately $-24°$. The equivalent yaw misalignment angles are negative because, for strong relative Coriolis forcing (low Rossby numbers), we observe that the Coriolis force deflects wind turbine wakes anti-clockwise. Therefore, for the Rossby number ($Ro = 125$) and ABL conditions simulated here, positive yaw misalignment and Coriolis-based wake deflections would be in opposition and would nearly cancel out, while negative yaw misalignment will enhance the inherent Coriolis-based anti-clockwise deflection. Future research should study the interactions of relative Coriolis forcing strength with wake steering control.

Previous studies that investigated Coriolis effects on wind turbine wakes have focused on turbines approximately half the size of modern offshore wind turbines, observing both clockwise and anti-clockwise wake deflections. Studying a rotor twice as large in diameter halves the relevant Rossby numbers for that turbine. For example, the NREL 5-MW turbine operating at rated wind speed sees a Rossby number $Ro \approx 880$. Our results suggest that in this operating regime, wakes for the NREL 5-MW reference turbine would deflect clockwise (van der Laan & Sørensen 2017), with a spread of deflection values (in magnitude and direction) due to turbulence which is dependent on the time averaging interval. However, as turbines become larger, Coriolis forces become more dynamically important, relative to the other terms in the lateral momentum balance. The next generation of turbines with rotors greater than 200 m in diameter will increasingly operate in regimes where the dynamics studied here is relevant, and wakes will be deflected increasingly anti-clockwise for lower Rossby numbers.

https://doi.org/10.1017/jfm.2025.35 Published online by Cambridge University Press

5. Summary and conclusions

The presence of Coriolis forces in the ABL affects wind turbine wake dynamics. Previous investigations have studied the interaction between turbine wakes and Coriolis forces for a relatively small range of rotor diameter-based Rossby numbers ($Ro = G/(f_c D)$). As wind turbine rotors increase in size, the wake structures that they create in the ABL also grow, resulting in more dynamically active Coriolis forcing. We explore a Rossby number range relevant to the next generation of offshore wind turbines using dimensions from the IEA 15-MW turbine for reference.

In this study, large eddy simulations of a single actuator disk-modelled wind turbine are used to explore the parametric effects of Coriolis forces on wind turbine wake dynamics in uniform and boundary layer inflow. Using a streamtube control volume, the lateral momentum budget is linked with observations of wake deflection. In uniform inflow conditions, the Coriolis force causes wakes to deflect anti-clockwise. When scaled by the Rossby number, wake dynamics in uniform inflow are shown to collapse, and non-negligible lateral pressure gradients partially oppose the direct Coriolis forcing. Lateral pressure gradients arise due to the formation of a counter-rotating vortex pair in uniform inflow and limit the wake deflection magnitude. For uniform inflow, neglecting the lateral pressure gradient forcing leads to an order-of-magnitude overprediction in wake deflection.

For TNBL and CNBL inflow, wake deflection also monotonically increases with decreasing Rossby number, becoming increasingly anti-clockwise. At high Rossby numbers (weak Coriolis forcing strength relative to inertial forces), wakes are deflected clockwise due to the effects of wind speed and direction shear that stem from Coriolis effects on the background ABL flow, in agreement with previous studies that have investigated high-Rossby-number regimes. At low Rossby numbers, wakes are deflected anti-clockwise. In the simulations presented here, we observe a transition between clockwise wake deflection to anti-clockwise wake deflection between $Ro = 500$ and $Ro = 250$. The transition point will depend on the ABL inflow conditions, such as the surface roughness, and wind turbine design and control strategy (e.g. thrust coefficient), which should be studied in future work. Unlike in uniform inflow, for ABL simulations, the dynamically active terms in the lateral momentum budget change as a function of streamwise position. Additionally, the lateral pressure gradient contribution is non-negligible and changes with the wake dynamics. In the TNBL, as well as in the CNBL when gravity waves are not present, the sign of the pressure gradient forcing term changes when the Reynolds stress divergence overtakes the Coriolis forcing term. In the CNBL, gravity waves are triggered when the boundary layer height interacts with the upper tip of the rotor area. Gravity waves considerably alter the dynamics of the lateral advection; in the present simulations, the presence of gravity waves increases the wake deflection in the CNBL compared with the TNBL or uniform inflow. While shallow CNBLs may be relatively uncommon in the environment, it is certainly possible that for stable boundary layers, large modern wind turbines could directly interact with the free atmosphere and trigger gravity waves. We recommend that future work studies the effects of gravity waves induced by stand-alone turbines.

This study is focused on neutrally stratified ABLs to limit the complexity of the parameter space and focus on Coriolis effects on wind turbine wakes. Thermal stratification, which, similar to Coriolis effects, alters the structure of wind shear and turbulence in the ABL, also affects wake dynamics (e.g. Abkar & Porté-Agel 2015). Further, only the vertical component of Earth's rotation is considered in this work, while the horizontal component has been shown to affect ABL development and vertical

https://doi.org/10.1017/jfm.2025.35 Published online by Cambridge University Press

transport of Reynolds stresses (Howland *et al.* 2020). Future work should consider the joint effects of Coriolis and buoyancy effects on wake dynamics. Additionally, we only simulate one surface roughness value representative of offshore wind conditions. Finally, future work should investigate the effects of Coriolis forcing on wind farm wake dynamics to explore the effects of wake superposition in varying Rossby number regimes. Understanding these effects will improve future wake models and influence wind farm design and control.

Acknowledgements. The authors acknowledge funding from the National Science Foundation (Fluid Dynamics program, grant number FD-2226053). In addition, K.S.H. acknowledges funding through a National Science Foundation Graduate Research Fellowship under grant no. DGE-2141064. Simulations were performed on Stampede2 and Stampede3 supercomputers under the NSF ACCESS project ATM170028.

Declaration of interests. The authors report no conflict of interest.

Appendix A. Large eddy simulation numerical details

To solve the filtered, incompressible Navier–Stokes equations (2.1) to (2.3), copied below for convenience, we use the open-source incompressible flow solver PadéOps (https://github.com/Howland-Lab/PadeOps) (Ghate & Lele 2017; Howland *et al.* 2020).

$$\frac{\partial \tilde{u}_i}{\partial x_i} = 0, \tag{A1}$$

$$\frac{\partial \tilde{u}_i}{\partial t} + \tilde{u}_j \frac{\partial \tilde{u}_i}{\partial x_j} = -\frac{\partial \tilde{p}^\star}{\partial x_i} + \frac{\delta_{i3}}{\theta_0 Fr^2}(\tilde{\theta} - \langle \tilde{\theta} \rangle_{xy}) - \frac{\partial \tau_{ij}^d}{\partial x_j} - \frac{1}{Ro}\varepsilon_{ij3}(G_j - \tilde{u}_j) + f_{t,i}, \tag{A2}$$

$$\frac{\partial \tilde{\theta}}{\partial t} + \tilde{u}_j \frac{\partial \tilde{\theta}}{\partial x_j} = \frac{\partial q_j}{\partial x_j}. \tag{A3}$$

The flow is uniformly discretised on a staggered grid with the first vertical grid point located at $\Delta_z/2$ above the ground, where Δ_z is the grid spacing in the wall-normal direction. Fourier collocation is used in the horizontal directions while a sixth-order staggered compact finite difference scheme is used in the wall-normal direction (Nagarajan *et al.* 2003). De-aliasing is performed with the 3/2 rule (Canuto *et al.* 1988). A fourth-order Runge–Kutta method is used for time integration (Gottlieb *et al.* 2011) using a Courant–Friedrichs–Lewy number of 1.0.

The subgrid stress tensor $\tau_{ij} = \widetilde{u_i u_j} - \tilde{u}_i \tilde{u}_j$ and subgrid heat flux $q_j = \widetilde{u_j \theta} - \tilde{u}_j \tilde{\theta}$ are modelled with the grid-resolved velocity and potential temperature fields. A subgrid eddy viscosity is used to model the deviatoric component of the subgrid stresses $\tau_{ij}^d = \tau_{ij} - \frac{1}{3}\delta_{ij}\tau_{kk} = -2\nu_{SGS}\tilde{S}_{ij}$, where $\tilde{S}_{ij} = \frac{1}{2}(g_{ij} + g_{ji})$ is the resolved strain rate tensor and $g_{ij} = \partial \tilde{u}_i / \partial x_j$ is the resolved velocity gradient tensor. The isotropic component of the subgrid stress tensor is absorbed into the resolved modified pressure $\tilde{p}^\star$. In the sigma subgrid-scale (SGS) model, Nicoud *et al.* (2011) model subgrid eddy viscosity ν_{SGS} as

$$\nu_{SGS} = (C_\sigma \Delta)^2 \frac{\sigma_3(\sigma_1 - \sigma_2)(\sigma_2 - \sigma_3)}{\sigma_1^2}, \tag{A4}$$

where σ_1, σ_2 and σ_3 are the singular values of g_{ij}, Δ is the grid size, and C_σ is the model coefficient. We select $C_\sigma = 0.9$ in our simulations, which yields excellent agreement with CNBL validation cases from Liu *et al.* (2021). The subgrid heat flux also uses an eddy

https://doi.org/10.1017/jfm.2025.35 Published online by Cambridge University Press

viscosity closure where

$$q_j = -\frac{\nu_{SGS}}{Pr_{SGS}} \frac{\partial \tilde{\theta}}{\partial x_j}. \tag{A5}$$

A turbulent Prandtl number $Pr_{SGS} = 0.4$ is used (Li 2019; Howland *et al.* 2020). Additional CNBL simulations show that for $Pr_{SGS} \in [0.4, 0.7]$, profiles of horizontally averaged velocity magnitude $U(z)$ differ less than 0.5 % (not shown).

Periodic boundary conditions are used in the streamwise and lateral directions. Numerical details for the concurrent-precursor numerical set-up (Stevens *et al.* 2014), which is used to simulate a non-periodic, finite wake in the streamwise direction, are given in Appendix A.2. For simulations of the ABL (not uniform inflow conditions), a wall model is used at the bottom boundary. The wall stress is prescribed using Monin–Obukhov similarity theory for neutral boundary layers (Moeng 1984):

$$\tau_{13}|_w = -\left(\frac{\kappa\sqrt{\tilde{u}_1^2 + \tilde{v}_1^2}}{\log(0.5\Delta_z/z_0)}\right)^2 \frac{\tilde{u}_1}{\sqrt{\tilde{u}_1^2 + \tilde{v}_1^2}}, \tag{A6}$$

$$\tau_{23}|_w = -\left(\frac{\kappa\sqrt{\tilde{u}_1^2 + \tilde{v}_1^2}}{\log(0.5\Delta_z/z_0)}\right)^2 \frac{\tilde{v}_1}{\sqrt{\tilde{u}_1^2 + \tilde{v}_1^2}}, \tag{A7}$$

where $\tilde{u}_1$ and $\tilde{v}_1$ are filtered velocities at the first vertical level ($0.5\Delta_z$) in the streamwise and lateral directions and $\kappa = 0.4$ is the von Kármán constant. The friction velocity can be computed from the wall shear stress using $\tau_{13}|_w = u_*^2 \cos(\alpha_0)$ and $\tau_{23}|_w = u_*^2 \sin(\alpha_0)$, where $\alpha_0 = \arctan(\tilde{v}_1/\tilde{u}_1)$ is the wind angle at the first grid point. No stability correction is needed in neutral boundary simulations as the heat flux at the wall is set to zero ($q_3|_w = 0$). Slip walls are prescribed with zero vertical velocity ($\tilde{w} = 0$) and zero vertical gradient. The tildes $\tilde{(\cdot)}$ are dropped for convenience for the remainder of this appendix.

A.1. *Actuator disk model*

The wind turbine is implemented as an actuator disk model (ADM) introduced by Calaf *et al.* (2010) and further developed by Shapiro *et al.* (2019). The ADM exerts a force normal to the disk face that is proportional to the disk-averaged velocity u_d. The magnitude of the thrust force is computed $F_T = (1/2)\rho A_d u_d^2 C_T'$, where ρ is air density, $A_d = \pi D^2/4$ is the area of the ADM and C_T' is the thrust coefficient of the turbine (Calaf *et al.* 2010). A local thrust coefficient $C_T' = 1.33$ is used in all simulations, which corresponds to $C_T = 3/4$ following one-dimensional momentum theory. The thrust coefficient is held fixed, and not modified as a function of the incident wind speed in this study. The forcing is distributed over a Gaussian smoothing kernel $\mathcal{R}(x, y, z)$ given by Shapiro *et al.* (2019) to reduce numerical oscillations in the flow fields. For all simulations, the smoothing filter width $\Delta_s = 2.5h$ is used, where $h \equiv (\Delta_x^2 + \Delta_y^2 + \Delta_z^2)^{1/2}$ and Δ_{x_i} is the grid spacing in the x_i direction. The thrust correction factor derived by Shapiro *et al.* (2019) is not used because C_T' and grid resolution are constant across all simulations.

A.2. *Concurrent-precursor set-up*

To simulate a finite-length wake that is not recycled into the inlet of the simulation through the use of periodic boundary conditions, we follow the concurrent-precursor numerical

https://doi.org/10.1017/jfm.2025.35 Published online by Cambridge University Press

set-up from Stevens *et al.* (2014). A fringe region (Nordström *et al.* 1999) is used in the final 25 % of the domain in the streamwise direction to replenish momentum lost in the wake region. The fringe forcing appears as an additional forcing term on the right-hand side of (A2). A penalty force proportional to the difference between the flow velocity in the primary simulation and the target velocity is applied in the primary simulation:

$$f_i^{\mathrm{fr}}(x_j, t) = -s^{\mathrm{fr}}(x)(u_i(x_j, t) - u_i^B(x_j, t)), \tag{A8}$$

where $s^{\mathrm{fr}}(x)$ is the magnitude of the forcing function which ranges from 0 in the usable domain (outside the fringe) to a maximum of λ inside the fringe (Nordström *et al.* 1999). In ABL simulations, the target velocity $u_i^B(x_j, t)$ derives from an empty ABL simulation without a turbine which is run concurrently with equal time stepping. For the case of uniform inflow, the fringe target velocity is $u_i^B = (G, 0, 0)$. The parameter $\lambda = \lambda^{\mathrm{fr}}/\Delta t$ is controlled by a free parameter λ^{fr} and scaled by the time step Δt. The time-averaged streamwise velocity differs less than 1.5 % in the usable domain for $\lambda^{\mathrm{fr}} \in [0.05, 1]$, compared with a simulation of doubled domain length L_x. The conclusions are unaffected by the choice of λ^{fr} as shown in Appendix A.5, showing robustness in the concurrent-precursor set-up. Fringe forcing is also added to the potential temperature equation (A3) with θ and θ^B in place of u_i and u_i^B to restore temperature perturbations in the primary domain.

A.3. *Rayleigh damping layer*

A Rayleigh damping layer (RDL) absorbs waves in the top 25 % of the domain (Klemp & Lilly 1978). The RDL is similar to the fringe described in Appendix A.2 and takes the form

$$f_i^{\mathrm{ra}}(x_j, t) = -\nu(z)(u_i(x_j, t) - G_i), \tag{A9}$$

where $\nu(z)$ is the magnitude of the RDL and G_i is the prescribed geostrophic wind. The function form of $\nu(z)$ follows Klemp & Lilly (1978) and smoothly transitions from zero at the top of the free atmosphere $z = 0.75L_z$ to $\nu_{\max} = 0.025/\Delta t$ at the top of the domain $z = L_z$.

A.4. *CNBL and TNBL validation*

To validate our numerical approach, we perform additional simulations matching cases published by Liu *et al.* (2021) and Jiang *et al.* (2018). Liu *et al.* (2021) sweep over varying inversion strengths and latitudes to change the CNBL development. Using PadéOps, we simulate the CNBL of varying inversion strength using a domain size $2\pi \times 2\pi \times 2\,\mathrm{km}^3$ and a grid resolution of 288^3 points consistent with Liu *et al.* (2021). The surface roughness is $z_0 = 10^{-4}$ m, geostrophic wind speed is $G = 12\,\mathrm{m\,s}^{-1}$, and latitude is $\phi = 70°$, and the free-atmosphere lapse rate $\Gamma \in [1, 3, 9]\,\mathrm{K\,km}^{-1}$ is varied between simulations. Overall, we observe excellent agreement in horizontally averaged, time-averaged wind magnitude $U(z)$ and potential temperature $\theta(z)$, as shown in figure 18. The wind speed magnitude $U(z)$ is always within 2 % compared with validation data and the relative mean absolute error (MAE) against the validation simulations is less than 0.4 %.

For the TNBL, we compare with LES of the truly neutral (Ekman) boundary layer from Jiang *et al.* (2018) following their numerical set-up. While Jiang *et al.* (2018) use a stretched vertical grid where spacing gradually increases with altitude ($\Delta z_{i+1}/\Delta z_i \approx 1.03$), we simulate a vertical domain with constant vertical spacing. As such, we simulate three different vertical spacing levels for Δ_z: 12 m, matching TNBL simulations in § 2, 6 m

https://doi.org/10.1017/jfm.2025.35 Published online by Cambridge University Press

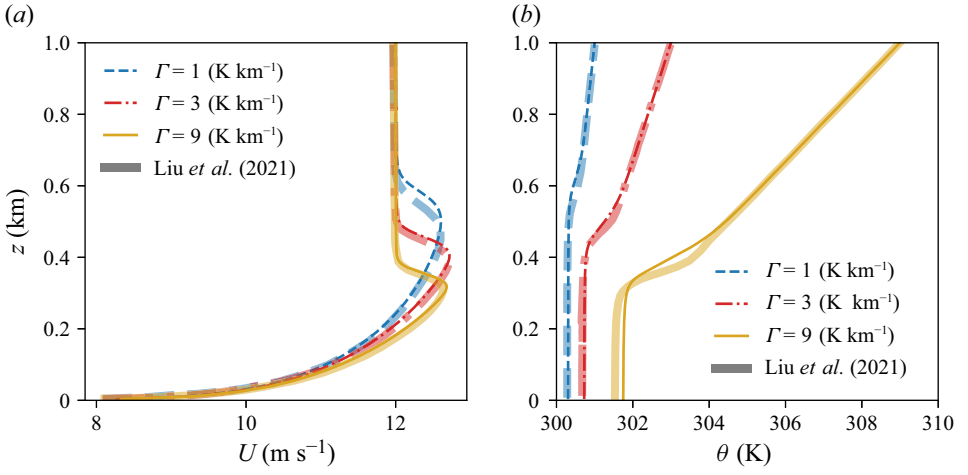

Figure 18. Numerical validation of the CNBL against data from Liu *et al.* (2021) showing horizontally and time-averaged (*a*) velocity and (*b*) temperature profiles for varying free-atmosphere lapse rate Γ.

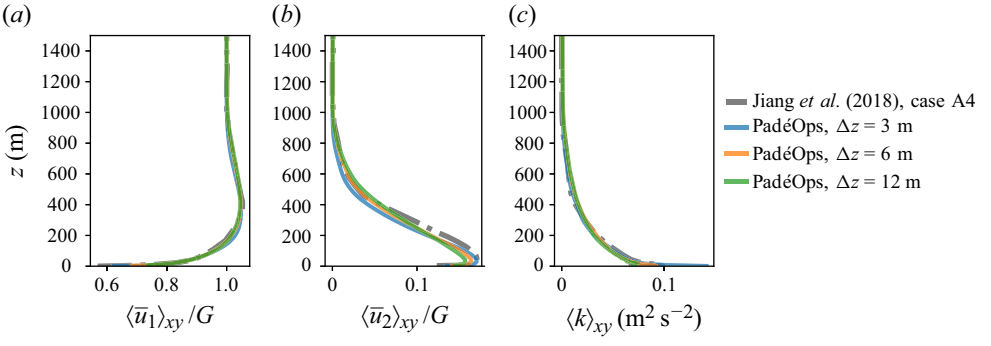

Figure 19. TNBL validation simulations compared with data from Jiang *et al.* (2018) varying vertical resolution, showing time-averaged, horizontally averaged (*a*) streamwise velocity u_1, (*b*) lateral velocity u_2 and (*c*) turbulence kinetic energy $k = \frac{1}{2}\overline{u_i' u_i'}$.

and 3 m. The vertical domain height is $L_z = 2$ km in both cases. The surface roughness z_0 is 2×10^{-4} m and the latitude is $\phi = 43.3°$. A horizontal resolution of $\Delta_x = \Delta_y = 16$ m is used in all PadéOps simulations. In all cases, we find close agreement in the wind speed profiles with LES from Jiang *et al.* (2018), as shown in figure 19. The near-wall wind direction and turbulence kinetic energy approach reference values when the grid resolution is refined.

A.5. *Sensitivity of wake dynamics to the numerical set-up*

To evaluate the sensitivity of the wake evolution to the numerical set-up, we run a variety of additional simulations. These include adjustments to the domain size, doubling the grid resolution, varying the magnitude of the fringe parameter λ^{fr} and perturbing the wind inflow angle. The wake deficit, computed as a streamtube-average of the velocity deficit $\Delta\bar{u}$ and the wake deflection (with the linearised mean advection at hub height $x\psi_{hub}$ subtracted, as in figure 13) are shown in figure 20. Overall, we observe a small sensitivity to the inflow angle ψ_{hub}, which inherently drifts due to inertial oscillations. Doubling the streamwise domain size while keeping Δ_x constant allows for larger flow structures

https://doi.org/10.1017/jfm.2025.35 Published online by Cambridge University Press

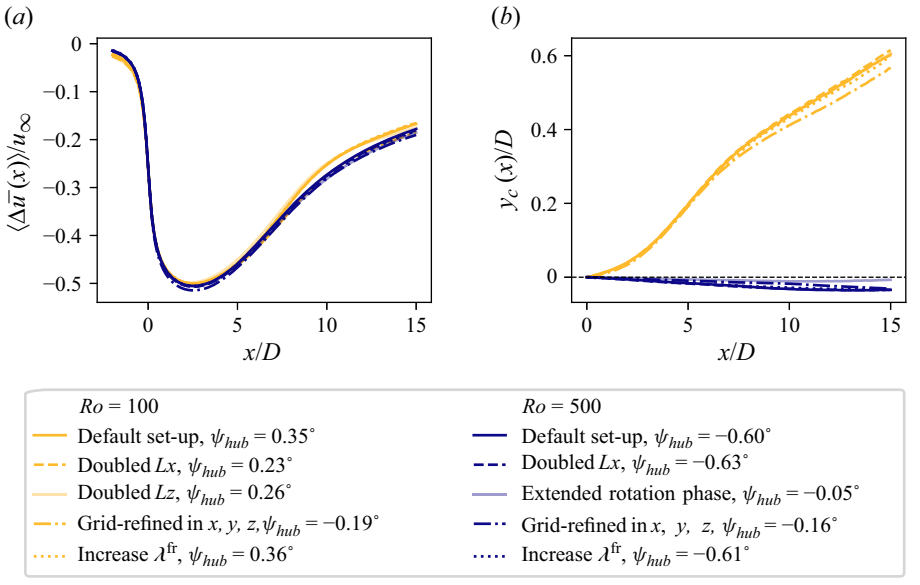

Figure 20. Sensitivity to the numerical set-up in the CNBL between $Ro = 500$ and $Ro = 100$ for (*a*) streamtube-averaged wake velocity deficit and (*b*) wake deflection computed using the centroid of the streamtube.

to develop in the precursor ABL. We increase L_z in the low-Rossby-number case, where gravity waves are observed, to evaluate the impact of gravity wave reflection on the wake dynamics. Doubling the vertical domain height reduces the reflectivity, as measured by the ratio of vertical kinetic energy between downward and upward propagating waves (Taylor & Sarkar 2007; Lanzilao & Meyers 2024), from 23 % to 12 %. Despite this, the wake recovery and deflection remain essentially unchanged, indicating that wave reflection minimally impacts the wake dynamics studied here. The inflow wind angle has the largest impact on the wake deflection. For $Ro = 500$, wake deflections induced by Coriolis forces are equivalent to yaw misalignments magnitudes of $\approx 3°$, following the analysis defined in § 4.6. Therefore, wake deflections at higher Rossby numbers are more sensitive to the inflow angle direction than at low Rossby numbers. Nonetheless, the spread in wake deflections shown in figure 20(*b*) are still small compared with the variation in Rossby number.

Appendix B. Dependence on time averaging window

In the absence of friction, the free atmosphere behaves like an undamped harmonic oscillator. Perturbations from the geostrophic balance will cause inertial oscillations, which are periodic changes in the ABL structure that occur on time scales of $\approx 2\pi/f_c$ (Blackadar 1957; Stull 1988). In LES, inertial oscillations are introduced at the initialisation of the ABL and slowly decay due to damping from the ABL. However, we still observe changes in the wind speed of approximately ± 1 % and changes in wind direction of $\pm 0.5°$ throughout one inertial period. Therefore, we choose to time-average wake statistics over a time interval $T = 2\pi/f_c \approx 17$ h to avoid biasing results with statistics that contain a partial period of inertial oscillation.

The time averaging duration can be increased to any integer multiple of the inertial oscillation period. To check if our results are sensitive to the time averaging period, we

https://doi.org/10.1017/jfm.2025.35 Published online by Cambridge University Press

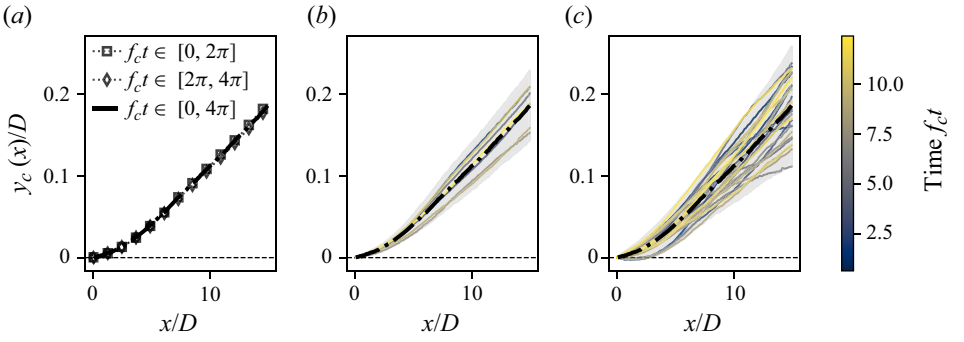

Figure 21. Sensitivity to time averaging for wake deflections at $Ro = 125$ in TNBL inflow. The dash-dotted line is time averaged over a double period of inertial oscillations. (*a*) Averaging over one inertial period (≈ 17 h) removes all scatter in the wake centroid data. (*b*) Wake deflections for 4-hour time averages. (*c*) Wake deflections for 1-hour time averages. In panels (*b*) and (*c*), the grey shaded region represents a $2\bar{\sigma}$ interval.

also perform a simulation for the $Ro = 125$ case in TNBL inflow over two inertial periods $4\pi/f_c \approx 34$ h. The comparison of wake deflections averaged over one and two inertial periods is shown in figure 22(*a*). We find that the quantitative wake deflection only changes by a maximum of 4 % at a location of $x = 5D$ when comparing the first inertial oscillation period to the second. Therefore, we find that a single inertial period of time averaging is sufficient for the statistics reported here. Additionally, we find that the wake recovery is less sensitive than the wake deflection to the averaging time, and we also find no significant difference in the residuals of the momentum budgets when averaging over a double period of inertial oscillations.

In § 4.6, one-hour time averages are used to show a band of possible wake deflections on time scales relevant to ABL dynamics and wind farm flow control. This band is computed with a width of twice the standard deviation $\bar{\sigma}$ of the ensemble of wake deflections as a function of downstream distance. Wake deflections measured in non-overlapping 4-hour and 1-hour time averages are shown in figures 21(*b*) and 21(*c*), respectively. As the averaging time increases, the variation in the observed range of deflections narrows around the mean value, which is averaged over a double inertial period. The time in which the averaging window ends is denoted by the colourbar for figure 21(*b*,*c*), where $t = 0$ corresponds to the time that the wake has fully developed and time averaging begins. The spread in colours between instances of wake deflection shows that the wake deflection predominately changes stochastically with ABL turbulence.

Appendix C. Streamtube analysis sensitivity

In this appendix, we compare the streamtube analysis of wake deflection to other wake deflection metrics. As discussed in § 3.2, using a streamtube as an analogue for the wake provides a physical and robust interpretation of the wake evolution. Throughout this paper, wake deflection y_c is defined as the centroid of the streamtube in the yz-plane (figure 2*b*). Other definitions of the wake deflection include the centroid of the wake velocity deficit at hub height, computed as

$$y_c(x) = \frac{\int y \Delta\bar{u}\, \mathrm{d}y}{\int \Delta\bar{u}\, \mathrm{d}y}, \tag{C1}$$

https://doi.org/10.1017/jfm.2025.35 Published online by Cambridge University Press

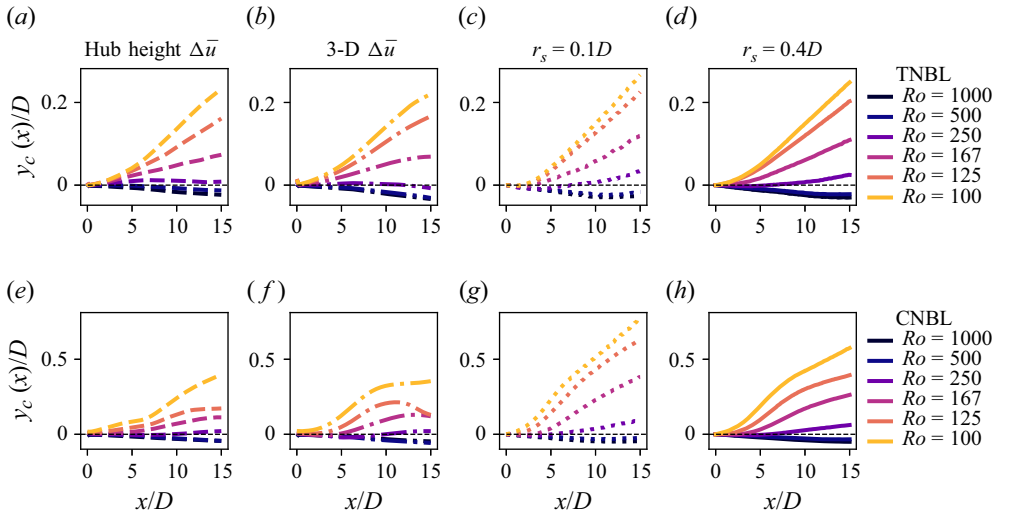

Figure 22. Wake centroid deflection in (*a–d*) TNBL inflow and (*e–h*) CNBL inflow for various definitions of the wake centre y_c. The wake center is given by (*a*,*e*) hub height centroid of $\Delta\bar{u}$ given by (C1), (*b*,*f*) three-dimensional centroid of $\Delta\bar{u}$ given by (C2), (*c*,*g*) streamtube centroid seeded at $r_s = 0.1D$, and (*d*,*h*) streamtube centroid seeded at $r_s = 0.4D$, which also is shown in figure 13.

or the centroid of the wake computed from a yz-cross-section of the wake (e.g. Howland *et al.* 2016)

$$y_c(x) = \frac{\iint y\Delta\bar{u}\,\mathrm{d}y\,\mathrm{d}z}{\iint \Delta\bar{u}\,\mathrm{d}y\,\mathrm{d}z}. \tag{C2}$$

Various definitions of the wake deflection are shown in figure 22. The definition of y_c given by (C1) is shown in figure 22(*a*,*e*) while the definition of y_c given by (C2) is shown in figure 22(*b*,*f*).

For all definitions of the wake deflection y_c, we observe that decreasing the Rossby number (increasing the relative importance of Coriolis forces) results in increasingly anti-clockwise wake deflections. Additionally, we observe a split between low Rossby number, Coriolis-favored anti-clockwise wake deflections, and high Rossby number, turbulence-favored clockwise wake deflections regardless of the definition of y_c used. For all cases, the transitional Rossby number is between $Ro = 500$ and $Ro = 250$.

We connect the observed wake deflections across ABL regimes with the lateral momentum budget in § 4.5. Integrating the lateral momentum budget recovers the lateral position (streamtube deflection), as we show in Appendix D. However, the reconstruction of the streamtube deflection figure 16(*a*,*b*) does not exactly match the streamtube position. This is because the streamwise velocity $\langle\bar{u}\rangle$ is used to transform temporal integration into spatial integration in x, but the streamwise velocity $\bar{u}$ varies within the streamtube due to wind shear in the ABL and the presence of the wake. Velocity shear has a smaller effect on the integrated reconstruction of the wake deflection for smaller streamtubes, as explained by the dispersive advection in the derivation of the integral reconstruction (Appendix D). The same analysis in figure 16(*a*,*b*) is shown in figure 23 for a streamtube seeded at $r_s = 0.1D$, showing excellent agreement between the streamtube deflection and the integration reconstruction from the momentum budgets. In other words, the error incurred in the integration of the momentum budget is primarily due to the spatial averaging of $\langle\bar{u}\rangle$ and not because of a residual in the lateral momentum budget from LES.

https://doi.org/10.1017/jfm.2025.35 Published online by Cambridge University Press

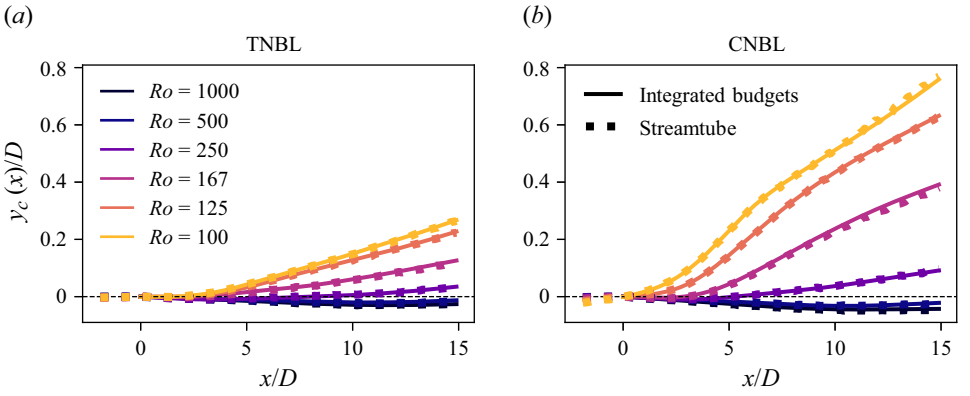

Figure 23. Same as figure 16(*a*,*b*) except using $r_s = 0.1D$ rather than $r_s = 0.4D$. Integrated budgets match the streamtube position more closely for the smaller streamtube radius. Dotted lines show the streamtube deflection for the smaller streamtube, and the solid lines show the integrated form of the lateral momentum budget.

Appendix D. Derivation of the integration of momentum budgets

The goal of this section is to derive the transformation between the streamtube-averaged momentum budget equations and the observations of streamtube-averaged velocity $\langle \bar{u} \rangle (x)$ and streamtube deflection $y_c(x)$. We take a Lagrangian perspective of fluid motion which follows an infinitesimally small parcel along a streamline trajectory seeded at the labelling position a_j at $\tau = 0$, where τ is the Lagrangian time. Newton's second law states that the sum of forces on the material volume representing the fluid parcel is equal to the change in its linear momentum. Written in terms of force per unit mass (f_i) as is consistent with the other equations in this paper, Newton's second law is given by

$$\frac{\partial u_{p,i}}{\partial \tau} = \sum f_i(r_{p,i}(\tau), \tau), \tag{D1}$$

where we use the subscript p in $u_{p,i}(\tau) = u_i(\tau; a_j)$ to represent the velocity of the parcel seeded at the labelling parameter a_j. As in previous equations in this study, the subscript i (j) denotes the direction of a tensor, such as the position and velocity vectors. In general, the force on the parcel at time τ depends on the position of the parcel $r_{p,i}(\tau) = r_i(\tau; a_j)$. The velocity of the parcel is the time derivative of the parcel position such that

$$u_{p,i}(\tau) = \frac{\partial r_{p,i}}{\partial \tau}. \tag{D2}$$

To solve (D1) from an initial position a_j and initial velocity $u_{p,i}(0)$, we need information about the right-hand side forcing terms. In this analysis, we assume that the field $f_i(x_j)$ is statistically steady and known *a priori* (i.e. time-averaged fields from turbulent ABL flow). This is because we aim to reconstruct the streamline trajectory $r_{p,i}(\tau)$ from the forcing field f_i, rather than write a functional form for the right-hand side forcing terms. When given the right-hand side forcing terms which are provided in (3.2) and (3.3) for the x and y directions, respectively, (D1) and (D2) can be numerically integrated forward in time to solve for the streamline velocity and position. A change of variables from temporal integration to spatial integration is given by (D2) in the $i = 1$ direction such that $d\tau = (u_p(\tau))^{-1}\,\mathrm{d}x$ as long as the streamwise parcel velocity $u_p = u_{p,1}$ never changes sign, which is true for the flows described in this study. This change of variables also indicates that there exists a nonlinear transformation $\tau \to x$, where x is the streamwise coordinate in an Eulerian coordinate system. Under the spatiotemporal transformation $\tau \to x$, the

https://doi.org/10.1017/jfm.2025.35 Published online by Cambridge University Press

position of the streamline can be written $r_{p,i}(\tau) = (x(\tau), y_p(x(\tau)), z_p(x(\tau))$, where the functions $y_p(x)$ and $z_p(x)$ are yet unknown. Note that $x_p(x(\tau)) = x$ because there is no coordinate transformation between the Lagrangian and Eulerian frames of reference. Then, an expression for the streamline velocity can be written by combining (D1) and (D2) and applying the change of variables $\tau \to x$ such that

$$u_p(x)\frac{\partial u_{p,i}(x)}{\partial x} = \sum f_i(x, y_p(x), z_p(x)). \tag{D3}$$

To connect the integrated right-hand side forcing terms with the streamline position (and later, with the streamtube position), we can make (D3) an explicit expression for $u_{p,i}$ if the forcing on the parcel along the path of the streamline is also known *a priori*. That is, by assuming a known streamline path $y_p(x) = \tilde{y}_p(x)$, $z_p(x) = \tilde{z}_p(x)$ to evaluate the forcing terms f_i, we can reconstruct the velocity at the points along the streamline path by slightly modifying (D3) such that

$$u_p(x)\frac{\partial u_{p,i}(x)}{\partial x} = \sum f_i(x, \tilde{y}_p(x), \tilde{z}_p(x)). \tag{D4}$$

Integrating (D4) from $x_0 = x_p(\tau = 0)$ to x yields an expression for the streamline velocity:

$$u_{p,i}(x) = \sum \int_{x_0}^{x} \frac{1}{u_p(x')} f_i(x', \tilde{y}_p(x'), \tilde{z}_p(x'))\ \mathrm{d}x'. \tag{D5}$$

Note that the summation over the forcing terms has been moved outside of the integral to emphasise that contribution from each forcing term to $u_{p,i}(x)$ can be parsed separately. In the streamwise $i = 1$ direction, (D5) can be made explicit by using the identity $2u_p\partial u_p/\partial x = \partial(u_p)^2/\partial x$. After substitution into (D4), integrating yields

$$u_p(x) = \left[2\sum\left(\int_{x_0}^{x} f_x(x', \tilde{y}_p(x'), \tilde{z}_p(x'))\, dx'\right) + (u_p(x_0))^2\right]^{1/2}. \tag{D6}$$

Next, we derive the integration reconstruction of the parcel position. In particular, we are interested in the lateral deflection $y_p(x)$ induced by $f_y(x, y, z)$. We apply the change of variables to (D2) in the $i = 2$ direction to yield an expression for the lateral parcel velocity $u_{p,2}(x) = v_p(x)$:

$$v_p(x) = u_p(x)\frac{\partial y_p}{\partial x}. \tag{D7}$$

Then, we substitute (D7) into (D5) and integrate in x which yields

$$y_p(x) = y_p(x_0) + \underbrace{\int_{x_0}^{x} \frac{v_p(x_0)}{u_p(x')}\ \mathrm{d}x'}_{\text{Base Advection}} + \sum \underbrace{\int_{x_0}^{x} \frac{1}{u_p(x')} \int_{x_0}^{x'} \frac{1}{u_p(x'')} f_y(x'', \tilde{y}_p(x''), \tilde{z}_p(x''))\, \mathrm{d}x''\ \mathrm{d}x'}_{\text{Individual forcing contributions}}. \tag{D8}$$

The result in (D8) shows the decomposition of the lateral position of the fluid parcel $y_p(x)$ into the initial condition, nonlinear advection from the velocity initial condition (we call this the base advection term) and individual forcing contributions.

Now, we transition from streamlines to streamtubes. Taking a streamtube as a bundle of streamlines, we can write the streamtube-average operator for any fluid property μ along

https://doi.org/10.1017/jfm.2025.35 Published online by Cambridge University Press

the streamline by averaging over all of the streamlines within the streamtube. Using the streamtube-average notation $\langle\cdot\rangle$ from § 3.2, we define $\langle\mu\rangle = \langle\mu(\tau; a_j)\rangle \forall a_j \in \Omega$, where Ω is the domain containing all streamline seed locations within the streamtube. Throughout this paper, we use $\Omega = \{(x, y, z)|x = 0, (y^2 + (z - z_h)^2) < r_s^2\}$ to seed wake streamtubes at the rotor plane with radius $r_s = 0.4D$. Recall that streamtube-averaging occurs over the yz-plane at a constant location x within the streamtube. Then, $\langle\mu\rangle$ is a function of x only, while $\mu = \mu(\tau; a_j) = \mu(x, y_p(x), z_p(x))$ is a function of all three spatial coordinates. We define the spatial heterogeneity in the yz-plane by decomposing the streamtube-averaged and deviatoric components such that within the streamtube, $\mu = \langle\mu\rangle + \mu''$. Again, μ'' is a function of all three spatial coordinates and is only valid within the streamtube.

Using the streamtube decomposition, we extend the equations derived for streamline integration reconstruction from the momentum budget equations to a streamtube. We begin with $\mu = u_i$ to compute the streamtube-averaged velocity field. Streamtube-averaging (D4) over all streamlines $a_j \in \Omega$, we obtain

$$\left\langle u_p(x, y_p(x), z_p(x)) \frac{\partial u_{p,i}}{\partial x} \right\rangle = \sum \langle f_i(x, \tilde{y}_p(x), \tilde{z}_p(x)) \rangle. \tag{D9}$$

Spatial averaging over the right-hand side forcing terms can be brought inside the summation, but the advective term on the left-hand side of (D9) is a nonlinear product of two velocities. Again, the goal of this derivation is to connect the time-averaged wake observations, such as the wake velocity deficit and wake deflection, to the time- and streamtube-averaged budgets. If we focused on the deflection of an individual streamline, spatial heterogeneity within the streamtube would not be relevant. However, here, we seek to understand properties of the three-dimensional wake as a whole, rather than individual streamlines. As such, we seek to write an expression for the streamtube-averaged velocity only using streamtube-averaged quantities (such as forcing terms). To accomplish this, we apply the streamtube decomposition to the nonlinear term in (D9) such that

$$\begin{aligned} \left\langle u(x, y, z) \frac{\partial u_i}{\partial x} \right\rangle &= \left\langle (\langle u(x, y, z)\rangle + u''(x, y, z)) \frac{\partial}{\partial x} (\langle u_i(x, y, z)\rangle + u_i''(x, y, z)) \right\rangle \\ &= \langle u(x, y, z)\rangle \frac{\partial \langle u_i\rangle}{\partial x} + \left\langle u''(x, y, z) \frac{\partial u_i''}{\partial x} \right\rangle, \end{aligned} \tag{D10}$$

where we switch the notation of $u_{p,i}(x, y_p(x), z_p(x)) \forall a_j \in \Omega$ to the Eulerian field $u_i(x, y, z)$ to denote field variables within the streamtube. The second right-hand side term in (D10) is the streamtube-averaged dispersive advection. The dispersive advection accounts for the non-uniformity in streamwise velocity u across the yz-cross-section within the streamtube. When the streamtube is small (see Appendix C), dispersion can be ignored and the streamtube-averaged nonlinear advection term can be approximated

$$\left\langle u(x, y, z) \frac{\partial u_i}{\partial x} \right\rangle \approx \langle u(x, y, z)\rangle \frac{\partial \langle u_i\rangle}{\partial x}. \tag{D11}$$

As a result, the streamtube-averaged streamwise velocity, which follows the same derivation as the streamline velocity, can be reconstructed from the right-hand side forcing terms as

$$\langle u\rangle(x) = \left[2 \sum \left(\int_{x_0}^{x} \langle f_x(x', y, z)\rangle \, \mathrm{d}x' \right) + (\langle u\rangle(x_0))^2 \right]^{1/2}. \tag{D12}$$

https://doi.org/10.1017/jfm.2025.35 Published online by Cambridge University Press

We emphasise that the streamtube-averaged streamwise right-hand side forcing terms from (3.2) appear on the right-hand side of (D12), which are also the averaged forces shown in figure 11.

Finally, we derive an expression for the streamtube centroid from the lateral right-hand side forcing terms, which is the average of the streamline positions y_p within the streamtube. We streamtube-average over (D7) to obtain a relation between the centroid position and the average lateral velocity:

$$\begin{aligned}\langle v\rangle &= \left\langle u(x,\,y,\,z)\frac{\partial y_p}{\partial x}\right\rangle \\ &= \left\langle (\langle u(x,\,y,\,z)\rangle + u''(x,\,y,\,z))\frac{\partial}{\partial x}(\langle y_p\rangle + y_p'')\right\rangle \\ &= \langle u\rangle\frac{\partial\langle y_p\rangle}{\partial x} + \left\langle u''(x,\,y,\,z)\frac{\partial y_p''}{\partial x}\right\rangle. \end{aligned} \tag{D13}$$

Again, if the streamtube is small, then the averaged advection is much larger than the dispersion, and the second right-hand side term in (D13) can be ignored. Then, the derivation for the streamtube centroid $y_c = \langle y_p\rangle$ follows the same steps as (D8). The final result is

$$y_c(x) = \underbrace{\int_{x_0}^{x}\frac{\langle v\rangle(x_0)}{\langle u\rangle(x')}\,dx'}_{\text{Base Advection}} + \underbrace{\sum\int_{x_0}^{x}\frac{1}{\langle u\rangle(x')}\int_{x_0}^{x'}\frac{1}{\langle u\rangle(x'')}\langle f_y(x'',\,y,\,z)\rangle\,dx''\,dx'}_{\text{Individual forcing contributions}}, \tag{D14}$$

where the initial wake centroid position $y_c(x_0)$ is zero in all cases because the centroid of Ω is centred about the rotor. The forcing terms f_y are the right-hand side terms in the lateral RANS equation (terms II–V in (3.3)). Because the forcing terms f_y are assumed to be steady, (D14) is equivalent for time-averaged flow fields $\bar{u}_i$, which is shown in (4.3).

Appendix E. ABL simulations with variable hub height

In addition to the controlled non-dimensional parameters for surface roughness z_0/D and stability $\mu = N/f_c$, wakes in the ABL depend on the position of the rotor relative to the ABL height. In this study, we fix $z_h = 150$ m to consider a realistic wind turbine in changing ABL conditions. As a result, the dimensionless hub height of the wind turbine $\xi = z_h/h$ varies, where h is the ABL height. In this appendix, we show wake deflection results for additional simulations in the TNBL where ξ is kept constant $\xi \approx 0.3$ by varying the turbine hub height. To keep ξ constant, the turbine hub height is adjusted accordingly such that $z_h = [150,\,220,\,480]$ m for Rossby numbers $Ro = [100,\,167,\,500]$, respectively. Note that a hub height of 480 m is unrealistically tall for practical application, but choosing smaller ξ would result in turbine hub heights where the bottom of the rotor impinges the ground. We choose the TNBL to perform these simulations, rather than the CNBL, to avoid inducing gravity waves induced by interactions between the rotor and the capping inversion layer.

Wake deflections are shown in figure 24(*a*). The wake deflection still changes in magnitude with Ro, but all wakes are deflected more anti-clockwise than simulations where $z_h = 150$ m is kept constant because the direct Coriolis forcing is only dependent on $Ro^{-1}(G_1 - \bar{u})$, which primarily depends on the thrust coefficient, while turbulence and wind direction shear (and hence entrainment of clockwise-turning momentum in the wake)

https://doi.org/10.1017/jfm.2025.35 Published online by Cambridge University Press

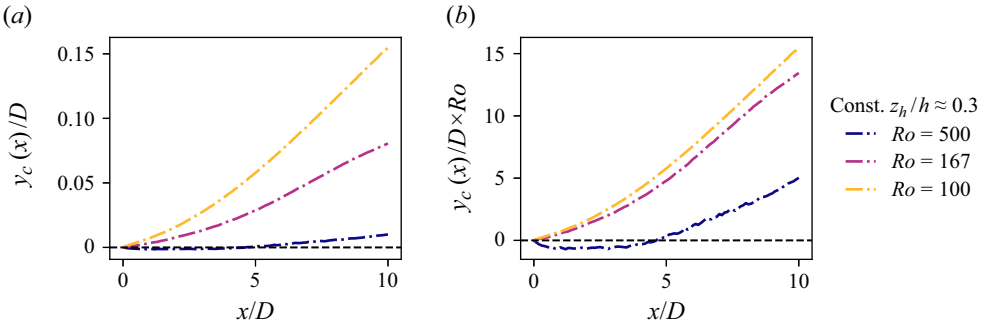

Figure 24. Wake deflections considering constant dimensionless hub height $z_h/h \approx 0.3$. (*a*) Streamtube wake deflection. (*b*) Wake deflections scaled by the Rossby number.

are reduced aloft. Scaling the wake deflections by the Rossby number in figure 24(*b*) does not collapse wake deflections onto one curve, as it does in uniform inflow, due to nonlinear scaling of the lateral turbulence fluxes with Ro even for constant ξ.

References

Abkar, M. & Porté-Agel, F. 2015 Influence of atmospheric stability on wind-turbine wakes: a large-eddy simulation study. *Phys. Fluids* **27** (3), 035104.

Abkar, M. & Porté-Agel, F. 2016 Influence of the Coriolis force on the structure and evolution of wind turbine wakes. *Phys. Rev. Fluids* **1** (6), 063701.

Abkar, M., Sørensen, J.N. & Porté-Agel, F. 2018 An analytical model for the effect of vertical wind veer on wind turbine wakes. In *Energies*, vol. **11**, Chap. 7. Multidisciplinary Digital Publishing Institute.

Allaerts, D. & Meyers, J. 2017 Boundary-layer development and gravity waves in conventionally neutral wind farms. *J. Fluid Mech.* **814**, 95–130.

Barthelmie, R.J., Frandsen, S.T., Nielsen, M.N., Pryor, S.C., Rethore, P.-E. & Jørgensen, H.E. 2007 Modelling and measurements of power losses and turbulence intensity in wind turbine wakes at Middelgrunden offshore wind farm. *Wind Energy* **10** (6), 517–528.

Barthelmie, R.J., Pryor, S.C., Frandsen, S.T., Hansen, K.S., Schepers, J.G., Rados, K., Schlez, W., Neubert, A., Jensen, L.E. & Neckelmann, S.2010 Quantifying the impact of wind turbine wakes on power output at offshore wind farms. *J. Atmos. Oceanic Technol.* **27** (8), 1302–1317.

Bastankhah, M. & Porté-Agel, F. 2016 Experimental and theoretical study of wind turbine wakes in yawed conditions. *J. Fluid Mech.* **806**, 506–541.

Blackadar, A.K. 1957 Boundary layer wind maxima and their significance for the growth of nocturnal inversions. *Bull. Am. Meteorol. Soc.* **38** (5), 283–290.

Bodini, N., Zardi, D. & Lundquist, J.K. 2017 Three-dimensional structure of wind turbine wakes as measured by scanning lidar. In *Atmospheric Measurement Techniques*, vol. **10**, chap. 8, pp. 2881–2896, Copernicus GmbH.

Calaf, M., Meneveau, C. & Meyers, J. 2010 Large eddy simulation study of fully developed wind-turbine array boundary layers. *Phys. Fluids* **22** (1), 015110.

Canuto, C., Hussaini, M.Y., Quarteroni, A. & Zang, T.A. 1988 *Spectral Methods in Fluid Dynamics*. Springer.

Churchfield, M.J. & Sirnivas, S. 2018 On the Effects of Wind Turbine Wake Skew Caused by Wind Veer, In 2018 Wind Energy Symposium, Kissimmee, Florida, American Institute of Aeronautics and Astronautics.

Churchfield, M., Wang, Q., Scholbrock, A., Herges, T., Mikkelsen, T. & Sjöholm, M. 2016 Using high-fidelity computational fluid dynamics to help design a wind turbine wake measurement experiment. *Journal of Physics: Conference Series* **753**, 032009.

Díaz, H. & Guedes Soares, C. 2020 Review of the current status, technology and future trends of offshore wind farms. *Ocean Engng* **209**, 107381.

Dörenkämper, M., Witha, B., Steinfeld, G., Heinemann, D. & Kühn, M. 2015 The impact of stable atmospheric boundary layers on wind-turbine wakes within offshore wind farms. *J. Wind Engng Ind. Aerodyn.* **144**, 146–153.

Ekman, V.W. 1905 On the influence of the earth's rotation on ocean-currents. *Arkiv för Matematik, Astronomi Och Fysik* **2** (11), 1–52.

https://doi.org/10.1017/jfm.2025.35 Published online by Cambridge University Press

ENGLBERGER, A., DÖRNBRACK, A. & LUNDQUIST, J.K. 2020 Does the rotational direction of a wind turbine impact the wake in a stably stratified atmospheric boundary layer?. In *Wind Energy Science*, vol. **5**, chap. 4, pp. 1359–1374.

FLEMING, P. *et al.*et al. 2019 Initial results from a field campaign of wake steering applied at a commercial wind farm – part 1. In *Wind Energy Science*, vol. **4**, chap. 2, pp. 273–285, Copernicus GmbH.

GADDE, S.N. & STEVENS, R. J.A.M. 2019 Effect of coriolis force on a wind farm wake. *Journal of Physics: Conference Series* **1256** (1), 012026.

GAERTNER, E. *et al.*et al. 2020 Definition of the IEA 15-megawatt offshore reference wind Turbine. Tech. Rep. NREL/TP-5000-75698., National Renewable Energy Lab (NREL), Golden.

GHATE, A.S. & LELE, S.K. 2017 Subfilter-scale enrichment of planetary boundary layer large eddy simulation using discrete Fourier–Gabor modes. *J. Fluid Mech.* **819**, 494–539.

GOIT, J.P. & MEYERS, J. 2015 Effect of ekman layer on windfarm roughness and Displacement height. In *Direct and Large-Eddy Simulation IX*. (ed. F.JOCHEN, K.HANS, J.G.BERNARD & A.VINCENZO), pp. 423–434, Springer International Publishing.

GOMEZ, S., MIGUEL, L., JULIE, K., MIROCHA, J.D. & ARTHUR, R.S. 2023 Investigating the physical mechanisms that modify wind plant blockage in stable boundary layers. In *Wind Energy Science*, vol. **8**, chap. 7, pp. 1049–1069, Copernicus GmbH.

GOTTLIEB, S., KETCHESON, D. & SHU, C.-W. 2011 *Strong Stability Preserving Runge-Kutta and Multistep Time Discretizations*. 1st edn edn. Wspc.

HECK, K.S., JOHLAS, H.M. & HOWLAND, M.F. 2023 Modelling the induction, thrust and power of a yaw-misaligned actuator disk. *J. Fluid Mech.* **959**, A9.

HOWLAND, M.F., BOSSUYT, J., MARTÍNEZ-TOSSAS, L.A., MEYERS, J. & MENEVEAU, C. 2016 Wake structure in actuator disk models of wind turbines in yaw under uniform inflow conditions. *J. Renew. Sustain. Ener.* **8** (4), 043301.

HOWLAND, M.F., GHATE, A.S. & LELE, S.K. 2018 Influence of the horizontal component of earth's rotation on wind turbine wakes. *J. Phys.: Conf. Ser.* **1037**, 072003.

HOWLAND, M.F., GHATE, A.S. & LELE, S.K. 2020 Influence of the geostrophic wind direction on the atmospheric boundary layer flow. *J. Fluid Mech.* **883**, A39.

HOWLAND, M.F., QUESADA, J.B., MARTÍNEZ, J.J.P., LARRA, N., PALOU, F., YADAV, N., CHAWLA, J.S., SIVARAM, V. & DABIRI, J.O. 2022 Collective wind farm operation based on a predictive model increases utility-scale energy production. *Nature Energy* **7** (9), 818–827.

HÖGSTRÖM, U., ASIMAKOPOULOS, D.N., KAMBEZIDIS, H., HELMIS, C.G. & SMEDMAN, A. 1988 A field study of the wake behind a 2 MW wind turbine. *Atmos. Environ. (1967)* **22** (4), 803–820.

IEA 2022 Renewables 2022. Paris: International Energy Agency, Tech. Rep.

JIANG, Q., WANG, S. & SULLIVAN, P. 2018 Large-eddy simulation study of log laws in a neutral ekman boundary layer. *J. Atmos. Sci.* **75** (6), 1873–1889.

JIMÉNEZ, Á., CRESPO, A. & MIGOYA, E. 2010 Application of a LES technique to characterize the wake deflection of a wind turbine in yaw. *Wind Energy* **13** (6), 559–572.

JONKMAN, J., BUTTERFIELD, S., MUSIAL, W. & SCOTT, G. 2009 Definition of a 5-MW reference wind Turbine for offshore system development. Tech. Rep. NREL/TP-500-38060, 947422.National Renewable Energy Lab. (NREL), Golden.

KLEMP, J.B. & LILLY, D.K. 1978 Numerical simulation of hydrostatic mountain waves. In *Journal of the Atmospheric Sciences*, vol. **35**, chap. 1, pp. 78–107, American Meteorological Society Section.

LANZILAO, L. & MEYERS, J. 2024 A parametric large-eddy simulation study of wind-farm blockage and gravity waves in conventionally neutral boundary layers. *J. Fluid Mech.* **979**, A54.

LI, D. 2019 Turbulent Prandtl number in the atmospheric boundary layer - where are we now? *Atmos. Res.* **216**, 86–105.

LIU, L., GADDE, S.N. & STEVENS, R.J.A.M. 2021 Geostrophic drag law for conventionally neutral atmospheric boundary layers revisited. *Q. J. R. Meteorol. Soc.* **147** (735), 847–857.

MAGNUSSON, M. & SMEDMAN, A.-S. 1994 Influence of atmospheric stability on wind turbine wakes. In *Wind Engineering*, vol. **18**, chap. 3, pp. 139–152, Sage Publications, Ltd.

MARTÍNEZ-TOSSAS, L.A., KING, J., QUON, E., BAY, C.J., MUDAFORT, R., HAMILTON, N., HOWLAND, M.F. & FLEMING, P.A. 2021 The curled wake model: a three-dimensional and extremely fast steady-state wake solver for wind plant flows. In *Wind Energy Science*, vol. **6**, chap. 2, pp. 555–570, Copernicus GmbH.

MEYERS, J., BOTTASSO, C., DYKES, K., FLEMING, P., GEBRAAD, P., GIEBEL, G., GÖÇMEN, T. & VAN-WINGERDEN, J.W. 2022 Wind farm flow control: prospects and challenges. In *Wind Energy Science*, vol. **7**, chap. 6, pp. 2271–2306, Copernicus GmbH.

https://doi.org/10.1017/jfm.2025.35 Published online by Cambridge University Press

MEYERS, J. & MENEVEAU, C. 2013 Flow visualization using momentum and energy transport tubes and applications to turbulent flow in wind farms. In *Journal of Fluid Mechanics*, vol. **715**, pp. 335–358, Cambridge University Press.

MOENG, C.-H. 1984 A large-eddy-simulation model for the study of planetary boundary-layer turbulence, In *Journal of the Atmospheric Sciences*, Vol. **41**, Chap. 13, pp. 2052–2062.American Meteorological Society Section.

MOHAMMADI, M., BASTANKHAH, M., FLEMING, P., CHURCHFIELD, M., BOSSANYI, E., LANDBERG, L. & RUISI, R. 2022 Curled-Skewed wakes behind yawed wind turbines subject to veered inflow. *Energies* **15** (23), 9135.

NAGARAJAN, S., LELE, S.K. & FERZIGER, J.H. 2003 A robust high-order compact method for large eddy simulation. *J. Comput. Phys.* **191** (2), 392–419.

NICOUD, F., TODA, H.B., CABRIT, O., BOSE, SA. & LEE, J. 2011 Using singular values to build a subgrid-scale model for large eddy simulations. *Phys. Fluids* **23** (8), 085106.

NORDSTRÖM, J., NORDIN, N. & HENNINGSON, D. 1999 The fringe region technique and the fourier method used in the direct numerical simulation of spatially evolving viscous flows. *SIAM J. Sci. Comput.* **20** (4), 1365–1393.

NOURI, R., VASEL-BE-HAGH, A. & ARCHER, C.L. 2020 The coriolis force and the direction of rotation of the blades significantly affect the wake of wind turbines. *Appl. Energ.* **277**, 115511.

OLIVARES-ESPINOSA, H., BRETON, S.-P., MASSON, C. & DUFRESNE, L. 2014 Turbulence characteristics in a free wake of an actuator disk: comparisons between a rotating and a non-rotating actuator disk in uniform inflow. *J. Phys.: Conf. Ser.* **555**, 012081.

POPE, S.B. 2000 Turbulent flows. Cambridge University Press.ISBN: 9780511840531

PRYOR, S.C., BARTHELMIE, R.J. & SHEPHERD, T.J. 2021 Wind power production from very large offshore wind farms. In *Joule*, vol. **5**, chap. 10, pp. 2663–2686, Elsevier.

QIAN, G.-W., SONG, Y.-P. & ISHIHARA, T. 2022 A control-oriented large eddy simulation of wind turbine wake considering effects of coriolis force and time-varying wind conditions. *Energy* **239**, 121876.

RAMPANELLI, G. & ZARDI, D. 2004 A method to determine the capping inversion of the convective boundary layer. *J. Appl. Meteorol.* **43** (6), 925–933.

ROSSBY, C.-G. & MONTGOMERY, R.B. 1935 The layer of frictional influence in wind and ocean currents. In *Papers in Physical Oceanography and Meterology*, vol. **3**, pp. 1–101, MIT Press.

SESCU, A. & MENEVEAU, C. 2014 A control algorithm for statistically stationary large-eddy simulations of thermally stratified boundary layers: a control algorithm for LES of thermally stratified boundary layers. *Q. J. R. Meteorol. Soc.* **140** (683), 2017–2022.

SHAPIRO, C.R., GAYME, D.F. & MENEVEAU, C. 2018 Modelling yawed wind turbine wakes: a lifting line approach. *J. Fluid Mech.* **841**, R1.

SHAPIRO, C.R., GAYME, D.F. & MENEVEAU, C. 2019 Filtered actuator disks: theory and application to wind turbine models in large eddy simulation. *Wind Energy* **22** (10), 1414–1420.

SORBJAN, Z. 1996 Effects caused by varying the strength of the capping inversion based on a large Eddy simulation model of the shear-free convective boundary layer. *J. Atmos. Sci.* **53** (14), 2015–2024.

STEVENS, R.J.A.M., GRAHAM, J. & MENEVEAU, C. 2014 A concurrent precursor inflow method for large eddy simulations and applications to finite length wind farms. *Renewable Energy* **68**, 46–50.

STEVENS, R.J.A.M., MARTÍNEZ-TOSSAS, L.A. & MENEVEAU, C. 2018 Comparison of wind farm large eddy simulations using actuator disk and actuator line models with wind tunnel experiments. *Renewable Energy* **116**, 470–478.

STULL, R.B. 1988 An introduction to boundary layer meteorology. Springer.

TAYLOR, J.R. & SARKAR, S. 2007 Internal gravity waves generated by a turbulent bottom Ekman layer. *J. Fluid Mech.* **590**, 331–354.

TENNEKES, H. 1973 A model for the dynamics of the inversion above a convective boundary layer. In *Journal of the Atmospheric Sciences*, vol. **30**, chap. 4, pp. 558–567, American Meteorological Society Section.

VAN DER LAAN, M.P., HANSEN, K.S., SØRENSEN, N.N. & RÉTHORÉ, P.-E. 2015 Predicting wind farm wake interaction with RANS: an investigation of the coriolis force. *J. Phys.: Conf. Ser.* **625**, 012026.

VAN DER, L., PAUL, M., BAUNGAARD, M. & KELLY, M. 2023 Brief communication: a clarification of wake recovery mechanisms. In *Wind Energy Science*, vol. **8**, chap. 2, pp. 247–254, Copernicus GmbH.

VAN DER, L., PAUL, M. & SØRENSEN, N.N. 2017 Why the coriolis force turns a wind farm wake clockwise in the Northern Hemisphere. In *Wind Energy Science*, vol. **2**, chap. 1, pp. 285–294, Copernicus GmbH.

VEERS, P. *et al.*et al. 2019 Grand challenges in the science of wind energy. *Science* **366** (6464), eaau2027.

VERMEULEN, P.E.J. 1980 An experimental analysis of wind turbine wakes. In3rd International Symposium on Wind Energy Systems, pp. 431–450.

https://doi.org/10.1017/jfm.2025.35 Published online by Cambridge University Press

WEI, D., WANG, N., WAN, D. & STRIJHAK, S. 2023 Parametric study of the effectiveness of active yaw control based on large eddy simulation. *Ocean Engng* **271**, 113751.

WYNGAARD, J.C. 2010 *Turbulence in the Atmosphere*. Cambridge University Press.

XIE, S. & ARCHER, C.L. 2017 A numerical study of wind-turbine wakes for three atmospheric stability conditions. *Boundary-Layer Meteorol.* **165** (1), 87–112.

ZAHLE, F., BARLAS, A., LØNBÆK, K., BORTOLOTTI, P., ZALKIND, D., WANG, L., LABUSCHAGNE, C., SETHURAMAN, L. & BARTER, G. 2024 *Definition of the IEA Wind 22-Megawatt Offshore Reference Wind Turbine*. Technical University of Denmark.

ZILITINKEVICH, S., ESAU, I. & BAKLANOV, A. 2007 Further comments on the equilibrium height of neutral and stable planetary boundary layers. *Q. J. R. Meteorol. Soc.* **133** (622), 265–271.

https://doi.org/10.1017/jfm.2025.35 Published online by Cambridge University Press